JETP Letters, Vol. 77, No. 11, 2003, pp. 599–602. From Pis'ma v Zhurnal Éksperimental'noĭ i Teoreticheskoĭ Fiziki, Vol. 77, No. 11, 2003, pp. 723–727.


# Screening and Antiscreening Effects in $J/\psi$ Production on Nuclei¶

**K. G. Boreskov and A. B. Kaidalov**

*Institute of Theoretical and Experimental Physics, Moscow, 117218 Russia*

*e-mail: boreskov@heron.itep.ru, kaidalov@heron.itep.ru*

Received April 15, 2003; in final form, April 28, 2003

Nuclear effects in $J/\psi$ hadro- and electroproduction on nuclei are considered in the framework of the reggeon approach. It is shown that the screening regime which holds for electroproduction at $x_F \gtrsim 0.7$ and for hadroproduction at $x_F \gtrsim -(0.2–0.4)$ changes with the antiscreening regime for smaller $x_F$ values. © *2003 MAIK "Nauka/Interperiodica".*

PACS numbers: 25.30.Rw; 25.43.+t; 11.55.Jy; 13.85.Ni; 24.85.+p

Heavy-quark production on nuclei provides important information on strong-interaction mechanisms and has been intensively discussed (see, e.g., [1–3] for review of experimental data, discussion of some phenomenological models, and for additional references). In this note we will discuss the phenomenon of changing the screening regime to an antiscreening one in $J/\psi$ hadro- and electroproduction when $x_\psi \equiv x_F$ decreases in the framework of the BCKT model [4, 5] based on the reggeon approach. For $J/\psi$ hadroproduction, this phenomenon happens in the region of negative $x_\psi$. An investigation of this region can provide important information on the dynamics of charmonium production and may allow discrimination of different dynamical models [2, 4, 6].

Nuclear effects are usually discussed in terms of conventional power-law parameterization $F_A(x_\psi) \propto F_N(x_\psi)A^{\alpha(x_\psi)}$, where $F_N(x_\psi)$ ($F_A(x_\psi)$) is the inclusive $J/\psi$ production cross section on a nucleon (on a nucleus). The function $\alpha(x_\psi)$ characterizes nuclear effects at different longitudinal momentum fraction $x_\psi$.

Experimental data on $J/\psi$ hadroproduction reveal a striking contradiction with the simplest theoretical expectations. Experimentally [7–9], the function $\alpha(x_\psi)$ decreases from 0.93–0.95 at $x_\psi \simeq 0$ to values ~0.75 at $x_\psi \simeq 0.8$, thus indicating an increase in absorption as $x_\psi$ increases. The formation-time mechanism predicts the opposite behavior. Instead of expected scaling with $p^{lab}_{J/\psi}$, experiment shows approximate Feynman scaling with $x_\psi$ [8]. Comparison of $J/\psi$ production data at different energies reveals an explicit breakdown of the QCD factorization theorem for this process [10].

On the other hand, when comparing the $x$ dependence of $\alpha$ for $J/\psi$ hadroproduction with that for light-quark particle hadroproduction (inclusive production of pions, nucleons, lambdas, etc.), one observes the same trend—small absorption at $x \simeq 0$, large absorption at $x \simeq 1$, and approximate Feynman scaling. The difference is only quantitative: $\alpha$ is about 0.4–0.5 at $x \simeq 1$ for light quarks instead of ~0.7 for heavy quarks. This behavior of $\alpha(x)$ for light hadrons allows a natural explanation by Regge theory. Small absorption at $x \sim 0$ is due to Abramovskii–Gribov–Kancheli (AGK) cancellation for inclusive spectra [11], and increased absorption at high $x$ is due to violation of AGK rules because of the momentum conservation requirement [12].

In [4], the model for heavy quark and lepton pair production was constructed taking into account the most essential aspects of the reggeon approach. In the spirit of a parton picture [13], it was suggested that a fast projectile, due to quantum-mechanical fluctuations, looks like a cloud of virtual particles consisting of light partons (quarks and gluons, or light-quark hadrons, mainly pions) and (with some small probability) heavy partons (say $c\bar{c}$ pair).[1] Different constituents of this fluctuation interact with nuclear matter and determine the dependence upon the atomic number $A$. There are both elastic and inelastic interactions which, from the viewpoint of reggeon diagrams, are different discontinuities of the same reggeon diagram. As a result, there exist definite numerical relations between discontinuities of different types (AGK rules [11]).

As was stressed in [4], one has to distinguish between two types of reggeon diagram cuttings. For diagrams of the first class, a registered particle is contained inside a pomeron and appears in the intermediate state only due to the cutting of this pomeron. In this

¶ This article was submitted by the authors in English.

[1] In reggeon theory, the mechanism for emitting these partons is supposed to be a multiperipheral one. Creation of heavy quarks in this model can be considered as an example of the "intrinsic charm" mechanism which was discussed by Brodsky *et al.* [14, 10]. In the reggeon approach, one can consider any heavy component on equal footing (e.g., "an intrinsic lepton pair" and so on).

case, the AGK rules are always valid and all of the contributions of many-pomeron diagrams to inclusive spectra cancel. This happens because each additional pomeron can be both cut and uncut, and, due to the opposite signs of inelastic and elastic rescatterings, they cancel. As a result, only the one-pomeron diagram contribution survives, giving the spectra a linear $A$ dependence. This situation is typical for low $x$ particles.

Another situation occurs if the particle to be registered is contained inside the "vertex" of a reggeon diagram (we use the term "vertex" for that part of the diagram that is common for several pomerons attached to it). In this case, AGK cancellation is generally not valid. The striking manifestation of this mechanism comes from the $A$ dependence of inclusive spectra at large $x$ close to 1 (momentum conservation mechanism [12]). The fastest particles belong to the "vertex" but not to the pomeron, and corresponding discontinuities give $\alpha \approx 1/3$ for large $A$ compared to $\alpha \approx 1$ for small $x$.

A similar effect exists if one observes a "vertex" particle of some particular type, e.g., the $J/\psi$ meson. There are two sources of nuclear effects in this case [4]. The first one is connected with rescatterings of light partons in fluctuation on different target nucleons or, alternatively, in the antilaboratory frame, with the fusion of fluctuations originating from different nucleons of a fast nucleus. This mechanism plays a small role at present energies $p_{lab} \lesssim 10^3$ GeV [4], and its contribution is inessential to the antiscreening effects that interest us.

Another contribution is connected to rescatterings of the charmed state itself. One of the important ingredients of the model of [4] is the assumption that it is not the $J/\psi$ meson that propagates along the nucleus but some primary colorless system containing both $c\bar{c}$ quarks (in the color state) and light quarks (to screen this color charge). This state, denoted as $X$, can be $D\bar{D}$ mesons, the $D^*\bar{D}^*$ state, or something else, but the crucial point is that this system is of large size and, therefore, strongly interacts with nucleons (with a cross section on the order of 20–30 mb). Only at the last stage does this $X$ system converts into a $J/\psi$ meson (or in $\psi'$), which is registered experimentally. Note that large nuclear effects in the observed $J/\psi$ production at $x \sim 1$ require a large nuclear absorption cross section for any model. In our model, these effects are due to large-distance nonperturbative dynamics.

After inelastic rescattering, the state $X$ can no longer be registered (e.g., due to conversion to a state with a small projection into $J/\psi$). One can describe this effect quantitatively by introducing a probability $\epsilon$ to find the state $X$ after its inelastic rescattering. Then, for $\epsilon = 1$, one has exact AGK cancellation; for $\epsilon = 0$, the situation is similar to the momentum conservation mechanism for light mesons when $x$ is close to 1 (no AGK cancellation) with $\alpha \simeq 1/3$; and, for $0 < \epsilon < 1$, the situation is an intermediate one with incomplete AGK cancellation. Moreover, the momentum of the state $X$ decreases after each inelastic rescattering. This redistribution of the longitudinal momentum of the state $X$ is essential for the antiscreening effects discussed below.

Let us denote the momentum fraction distribution of the $X$ system immediately after its production as $F_0(x)$. The state $X$ has a certain projection into the state $J/\psi$ (as well as into $\psi'$, etc.). The $x_\psi$ distribution can be obtained from $F_0(x)$ by convolution with some projection function $G_\psi$,

$$F_N^{(\psi)}(x_\psi) = F_1 \otimes G_\psi \tag{1}$$

where the following notation was used:

$$(f \otimes g)(x) = \int_x^1 \frac{dz}{z} f(z) g(x/z), \tag{2}$$

or, in the rapidity variables,

$$(f \otimes g)(\bar{y}) = \int_0^{\bar{y}} d\xi\, f(\xi) g(\bar{y} - \xi), \tag{3}$$

where $\bar{y} = Y - y$ is the rapidity in the antilab frame.

The $X$ state traveling through nuclear matter is subject to both elastic and inelastic rescatterings. As in [4], the change of the $x$ distribution due to inelastic rescattering will be described as a convolution with some function $\epsilon G(z)$, where $G(z)$ is normalized ($\int_0^1 G(z)dz/z = 1$), and the parameter $\epsilon$ determines the probability of again having the $X$ state after inelastic interaction (though with different momentum). After $k$ inelastic rescatterings of the state $X$, we have $k$-fold convolution:

$$F_k^{(\psi)} = F_1 \otimes \underbrace{\epsilon G \otimes \ldots \otimes \epsilon G}_{k \text{ times}} \otimes G_\psi. \tag{4}$$

It is essential that the operation of convolution be commutative and associative, so we first convolute $F_1$ with $G_\psi$ in Eq. (4) and thus get the $k$-fold convolution of the $J/\psi$ spectrum on the nucleon $F_N^\psi(x)$ with rescattering functions $G$:

$$F_k^{(\psi)} = F_N^\psi \otimes \underbrace{\epsilon G \otimes \ldots \otimes \epsilon G}_{k \text{ times}}. \tag{5}$$

In order to obtain the $J/\psi$ inclusive spectrum on a nucleus, the functions $F_k^{(\psi)}$ should be weighted with cross sections $\sigma_A^{(k+1)}$ for $k$ inelastic rescattering after $X$ production:

$$F_A^\psi = \sum_{k=0}^{\infty} F_k(x_\psi) \sigma_A^{(k+1)}. \tag{6}$$

The explicit form of the weights $\sigma_A^{(k+1)}$ depends upon the energy region [4]. However, the change $\sigma_A^{(k+1)}$ is rather smooth and for simplicity we will use the same low-energy expressions as in [4]:

$$\sigma_A^{(k+1)} = \sigma_{aN}^{(\psi)} \int d^2b \int_0^{T_A(b)} d\nu \exp(-\nu\sigma_X)(\nu\sigma_X)^k/k!, \quad (7)$$

where $\sigma_{aN}^{(\psi)}$ is the cross section of $J/\psi$ production on a nucleon, $\sigma_X$ is the cross section of interaction of the state $X$ with a nucleon, and $T_A(b)$ is two-dimensional nuclear density as a function of the impact parameter $b$ (nuclear profile). These formulas correspond to rescatterings ordered in the longitudinal direction (low-energy regime) and, after summation over $k$, give the well-known optical-type formula for the production cross section. Thus, we arrive at Eq. (6) for a $J/\psi$ nuclear inclusive cross section, where $F_k(x)$ and $\sigma_A^{(k+1)}$ are defined by Eqs. (5) and (7).

Let us discuss parameterizations of the distribution functions entering the model. The function $F_{aN}^{\psi}(x_\psi)$ can be determined from experimental data on $J/\psi$ production on a nucleon. Its form strongly depends on the projectile type $a$. For a hadron beam, it can be parameterized as

$$F_{aN}^{\psi}(x) = C_a(1-x)^{\beta_a}, \quad (8)$$

where $\beta_\pi \simeq 2$ for a pion and $\beta_p \simeq 3$ for a proton beam. For $J/\psi$ production by photons (and electrons), the form of this function is strongly different: the produced $\psi$ particles are concentrated near $x_\psi \simeq 1$, and the distribution over $x_\psi$ can be parameterized in a powerlike way:

$$F_{\gamma N}^{(\psi)}(x) = \beta_\gamma x^{\beta_\gamma}, \quad (9)$$

with $\beta_\gamma \geq 6$. We chose the value $\beta_\gamma = 6$.

As to the function $G(x)$, it is natural to suggest its similarity to the function $F_{\gamma N}^{(\psi)}(x)$. For simplicity, we choose the same form

$$G(x) = \beta x^{\beta}, \quad (10)$$

with $\beta$ considered as a free parameter.

The terms of the series (6) in the number of rescatterings $k$ decrease rapidly with $k$, and it is sufficient to take several first terms into account (4–5). The corresponding convolutions at fixed impact parameter $b$ are estimated analytically, and $b$ integration was performed numerically. We use for calculations the Woods–Saxon parameterization of the nuclear density, with standard values for the parameters taken from [15].

Before comparing theoretical predictions with experimental data, let us first discuss the qualitative character of the absorptive corrections. As discussed above, at small $x \approx 0$, we have AGK cancellation and the extent of its violation is proportional to $1-\epsilon$—the probability of losing the state $X$ after inelastic rescattering. The particle can be lost for registration not only if it disappears after interaction but also if it loses part of its momentum and is shifted into a different region in $x$. As a result, at large $x$ values, the AGK rules are violated and absorption effects can be observed (momentum conservation effect). However, this is only a redistribution (not a loss) of particles for the whole $x$ region. For a cross section integrated over the $x$ screening, (absorption) effects are connected only with the value $1-\epsilon$ and not with momentum conservation. For $J/\psi$ photoproduction, the absorption effects were usually analyzed only for an integrated cross section; this is a reason for the rather small values of the effective cross sections extracted for $J/\psi$ absorption (3–5 mb). We want to demonstrate here[2] that, as a function of $x$, nuclear effects can be rather large (with an effective cross section on the order of 20–30 mb) but, integrally, they cancel because of canceling contributions from screening and antiscreening regions.

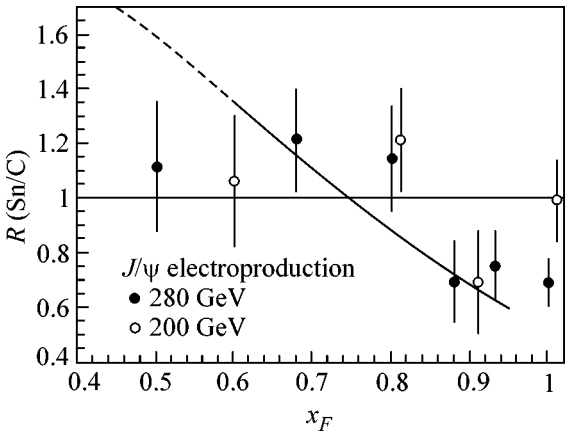


**Fig. 1.** Description of data [16] on ratio $R$(Sn/C) for $J/\psi$ electroproduction. The curve corresponds to model calculations at parameter values $\sigma = 30$ mb, $\epsilon = 0.85$, and $\beta = 12$.

This is demonstrated in Fig. 1, where we show a description of the NMC data [16] on the ratio $R$(Sn/Be) of $J/\psi$ electroproduction cross sections as a function of $x \equiv x_F$. Since, in this case, the $J/\psi$ spectrum is concentrated at $x$ close to 1, the antiscreening regime takes place even at $x \lesssim 0.8$. Note that theoretical predictions at small $x$ value ($x < 0.6$) are less reliable due to their sensitivity to small-$x$ parameterization of functions $F_{\gamma N}^{(\psi)}$ and $G(x)$. Let us mention that our model is valid only for nondiffractive inclusive $J/\psi$ production.

For $J/\psi$ hadroproduction, the antiscreening regime can be expected only for negative $x$. Figures 2a and 2b show that, for $J/\psi$ and $\psi'$ hadroproduction, the change

[2] This phenomenon was first discussed in the talk [5] based on our unpublished results.

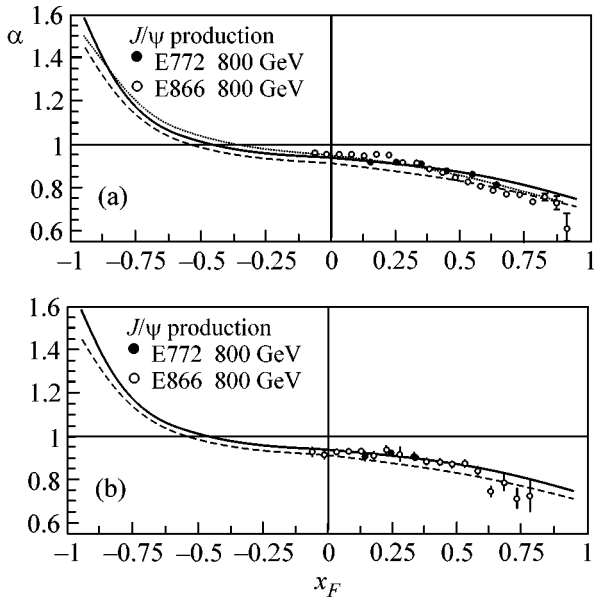


**Fig. 2.** (a) Description of data [7, 8] on nuclear dependence of $J/\psi$ hadroproduction. Curves correspond to model calculations for different methods of extraction: solid curve is from the ratio $R$(Fe/C), and dashed curve is from $R$(W/C). The dotted line extracted from $R$(W/C) corresponds to $\epsilon = 0.95$. (b) Description of data [7, 8] on the nuclear dependence of $\psi'$ hadroproduction. The curve corresponds to model calculations at parameter values $\sigma = 30$ mb, $\epsilon = 0.85$, $\beta = 12$.

of regime happens at $x \approx -(0.3–0.5)$. This value depends on parameters of the model—the less are the momentum losses (the larger is $\beta$) and the less is $\epsilon$, the more negative values of $x$ are necessary for the onset of antiscreening (see Fig. 2). For example, for the value of $\beta = 4$, the crossover happens even at $x \sim -0.2$.

It is important to note that it is not entirely adequate to analyze such a delicate effect as the variation of dependence on atomic number with a change of $x$ or $p_T$ in terms of the standard parameterizations $A^\alpha$. In general, $\alpha$ is not only a function of $x$ and $p_T$ but also depends on the atomic number $A$. This is demonstrated in Fig. 2: there is a noticeable difference of solid and dashed theoretical curves which correspond to different choices of $A$ ranges. Therefore, the $\alpha$ value obtained from experiments depends significantly on the chosen range of $A$ and on the method of analysis. To exclude this uncertainty, it is preferable to compare the ratios of the cross sections for different nuclei with theory.

For simplicity, we have considered only one primary state $X$. Under the approximation that all charmonia originate from this state, nuclear effects should be universal for $J/\psi$, $\psi'$, etc. In Fig. 2b, as an example we give a comparison of data on $\psi'$ hadroproduction from [7, 8] with model calculations with a single $X$ state at the same parameter values as in Fig. 2a. Generalization to several primary states can lead to different $A$ dependencies for different charmonia states.

Let us mention that, in some theoretical models [2, 6] used for the description of $J/\psi$, $\psi'$ hadroproduction in the negative $x$ region, the function $\alpha(x)$ decreases (screening effects increase) as $|x|$ increases in this region.

Thus, the experimental investigation of nuclear effects for charmonium production in the whole region of $x$ can provide valuable information for testing different dynamical models. In the reggeon approach, one can distinguish three different regions in the rapidity or in the Feynman variable for $J/\psi$ hadroproduction: in the central region, one has strong cancellation of screening diagrams and $\alpha$ is close to one (small absorption cross section); at $x > 0.2$, due to violation of the cancellation rule, the absorption effects increase and the effective cross section is about 20–30 mb; at negative $x$ less than $-(0.3–0.4)$, the antiscreening regime should be observed. Data on the $A$ dependence of charmonia production in the negative $x$ region will soon be available from the HERA-B experiment [17].

We are grateful to A. Capella and M. Danilov for stimulating discussions. This work was partially supported by RFBR grants no. 01-02-17383 and 00-15-96786, INTAS grant no. 00-00366, and DFG grant 436 RUS 113/721/0-1.

## REFERENCES

1. R. Vogt, Phys. Rep. **310**, 197 (1999).
2. R. Vogt, Phys. Rev. C **61**, 035203 (2000); Nucl. Phys. A **700**, 539 (2002).
3. B. Z. Kopeliovich and A. V. Tarasov, Nucl. Phys. A **710**, 180 (2002).
4. K. G. Boreskov, A. Capella, A. B. Kaidalov, and J. Tran Thanh Van, Phys. Rev. D **47**, 919 (1993).
5. K. G. Boreskov, in *Proceedings of XXII International Symposium on Multiparticle Dynamics*, Ed. by C. Pajares (World Sci., Singapore, 1993).
6. D. Koudela and C. Volpe, hep-ph/0301186.
7. D. M. Alde, H. W. Baer, T. A. Carey, *et al.*, Phys. Rev. Lett. **66**, 133 (1991); Phys. Rev. Lett. **66**, 2285 (1991).
8. M. J. Leith, W. M. Lee, M. E. Beddo, *et al.*, Phys. Rev. Lett. **84**, 3256 (2000).
9. R. Shahoyan, hep-ex/0207014.
10. R. Vogt, S. J. Brodsky, and P. Hoyer, Nucl. Phys. B **360**, 67 (1991).
11. V. A. Abramovskii, V. N. Gribov, and O. V. Kancheli, Yad. Fiz. **18**, 595 (1973) [Sov. J. Nucl. Phys. **18**, 308 (1974)].
12. A. Capella and A. Kaidalov, Nucl. Phys. B **111**, 477 (1976).
13. V. N. Gribov, in *Proceedings of the VII LIYF Winter School of Physics*, *Leningrad* (1973), Vol. 11, p. 5.
14. S. J. Brodsky and P. Hoyer, Phys. Lett. B **93**, 451 (1980).
15. A. Bohr and B. R. Mottelson, in *Nuclear Structure* (Benjamin, New York, 1969; Mir, Moscow, 1971), Vol. 1.
16. P. Amaudruz, M. Arneodo, A. Arvidson, *et al.*, Nucl. Phys. B **371**, 553 (1991).
17. HERA-B: Report on Status and Prospects, DESY-PRC 00/04.

JETP Letters, Vol. 77, No. 11, 2003, pp. 603–605. Translated from Pis'ma v Zhurnal Éksperimental'noĭ i Teoreticheskoĭ Fiziki, Vol. 77, No. 11, 2003, pp. 728–730.


# Refinement of the Hadronic Contribution to the Muon Anomalous Magnetic Moment and to $\alpha(M_z^2)$

**B. V. Geshkenbeĭn**

*Institute of Theoretical and Experimental Physics, ul. Bol'shaya Cheremushkinskaya 25, Moscow, 117259 Russia*
*e-mail: geshken@heron.itep.ru*

Received April 16, 2003; in final form, April 29, 2003

The contribution of the muon anomalous magnetic moment $a_\mu$(hadr) to the vacuum polarization and electromagnetic coupling constant $\alpha(q^2)$ for $q^2 = M_z^2$ is refined by using a new, more accurate value of the ρ-meson width. The values $a_\mu(\text{hadr}) = 678(7) \times 10^{-10}$ and $\delta\alpha_{\text{hadr}}(M_z^2) = 0.02786(6)$ were obtained in a QCD model with an infinite number of vector mesons. © *2003 MAIK "Nauka/Interperiodica".*

PACS numbers: 14.60.Ef; 13.40.Em

The purpose of this work is to refine the strong interaction contribution to the $a_\mu$(hadr) and $\delta\alpha_{\text{hadr}}(M_z^2)$ values obtained in [1, 2]. There are two reasons for such a calculation.

First, the new value [3, 4]

$$\Gamma_0^{ee} = (6.85 \pm 0.11)\ \text{keV} \tag{1}$$

was recently obtained for the electronic width of the ρ meson. This value is more accurate than the $\Gamma_0^{ee} = (6.77 \pm 0.32)$ keV used in [1] and $\Gamma_0^{ee} = (6.72 \pm 0.10)$ keV used in [2] and obtained in [5] by analyzing old measurements of the pion electromagnetic form factor.

Second, the function $R(s)$ is calculated by new formulas obtained in [6], where the proper analytic properties of the QCD polarization operators were taken into account in conjunction with the renormalization group. The function $R(s)$ for three flavors has the form

$$R(s) = \frac{3}{2}(1 + r(s)), \tag{2}$$

where the function $r(s)$ was calculated in [6] using the renormalization group and taking into account the absence of nonphysical singularities in the QCD polarization operators. All formulas for calculating $r(s)$ are given in [6].

The calculation of the hadronic contribution to the quantities $a_\mu$(hadr) and $\delta\alpha_{\text{hadr}}(M_z^2)$ [1, 2] is based on the QCD model with an infinite number of vector mesons, which was developed in [5, 7, 8]. This model satisfies all requirements of the Wilson operator product expansion, automatically includes nonperturbative effects [9], and is very useful for calculating integrals of the function

$$R(s) = \frac{\sigma(e^+e^- \longrightarrow \text{hadrons})}{\sigma(e^+e^- \longrightarrow \mu^+\mu^-)}. \tag{3}$$

In this model, the function $R(s)$ is written in the form

$$\begin{aligned} R(s) &= R_{ud}^{I=1}(s) \\ &+ R_{ud}^{I=0}(s) + R_s(s) + R_c(s) + R_b(s). \end{aligned} \tag{4}$$

Here, $R_{ud}^{I=1}$ and $R_{ud}^{I=0}$ describe the contributions of the $u$ and $d$ quarks in states with isospin $I = 1$ and 0 (ρ and ω families, respectively); $R_s(s)$, $R_c(s)$, and $R_b(s)$ present the contributions of $s$ (φ family), $c$ ($J/\varphi$ family), and $b$ (ϒ family) quarks, respectively. The narrow-resonance approximation, which applies if $\Gamma_k \ll M_k$ ($M_k$ is the mass of the $k$th resonance), is used. If $M_k\Gamma_k \gg M_k^2 - M_{k-1}^2$, then the function $R(s)$ is smooth beginning with the $k$th resonance, and all formulas of the narrow-resonance model are valid [10]. To calculate the integral of $R(s)$ in the QCD model with the infinite number of vector mesons, it is sufficient to know only the mass and electronic widths of several light resonances. In particular, for the ρ family, these are the ρ(770), ρ(1450), and ρ(1700) resonances. Compared to [1, 2], corrections associated with the new value of electronic width of the ρ meson are introduced only to $R_{ud}^{I=1}$. The changes in other families are negligible.

0021-3640/03/7711-0603$24.00 

The calculation of the hadronic contribution to the muon $(g-2)$ factor yields

$$a_\mu(\text{hadr}) = \frac{\alpha^2}{3\pi^2}\int\limits_{4m_\pi^2}^{\infty} ds K(s)R(s)/s = 678(7)\times 10^{-10}, \quad (5)$$

where

$$K(s) = x^2(1-x^2/2) + (1+x^2)(1+x^{-2}) \times [\ln(1+x) - x + x^2/2] + \frac{1+x}{1-x}x^2\ln x; \quad (6)$$
$$x = \frac{1-(1-4m_\mu^2/s)^{1/2}}{1+(1-4m_\mu^2/s)^{1/2}}.$$

The experimental value $a_\mu^{\text{exp}}$ obtained in [11–15] is equal to

$$a_\mu^{\text{exp}} = 11659203(8)\times 10^{-10}. \quad (7)$$

To compare the Standard Model predictions with the experiment, we divide $a^{\text{SM}}$ into different contributions

$$a_\mu^{\text{SM}} = a_\mu^{\text{QED}} + a_\mu^{\text{tot}}(\text{hadr}) + a_\mu^{\text{weak}}, \quad (8)$$

where

$$a_\mu^{\text{tot}}(\text{hadr}) = a_\mu(\text{hadr}) + a_\mu^{\text{HO}}(\text{hadr}) + a_\mu^{\text{LBL}}(\text{hadr}), \quad (9)$$

$a_\mu^{\text{QED}} = 116584706(3)\times 10^{-11}$ is the pure electromagnetic correction [16, 17], $a_\mu^{\text{HO}}(\text{hadr}) = -100(6)\times 10^{-11}$ is the $(\alpha/\pi)^3$-order hardon contribution [18, 19], $a_\mu^{\text{LBL}}(\text{hadr}) = 86(35)\times 10^{-11}$ is the contribution of the hadronic light-by-light scattering [20–22], and $a_\mu^{\text{weak}} = 154(3)\times 10^{-11}$ is the contribution of the weak interactions [23]. As a result, we obtain

$$a_\mu^{\text{SM}} = 1165916930(78)\times 10^{-11}, \quad a_\mu^{\text{exp}} - a_\mu^{\text{SM}} = 404(112)\times 10^{-11}, \quad (10)$$

i.e., $a_\mu^{\text{SM}}$ is less than the experimental value $a_\mu^{\text{exp}}$ by $3.6\sigma$.

The result given by Eqs. (5) and (10) should be compared with the recent most precise $a_\mu(\text{hadr})$ values calculated by integrating formula (5) with the cross sections measured for annihilation $e^+e^- \longrightarrow$ hadrons [24, 25]. According to [24],

$$a_\mu(\text{hadr}) = 6847(70)\times 10^{-11}, \quad a_\mu^{\text{exp}} - a_\mu^{\text{SM}} = 337(108)\times 10^{-11} \ [24]. \quad (11)$$

The $a_\mu^{\text{SM}}$ value is smaller by $3\sigma$ than the experimental value $a_\mu^{\text{exp}}$ obtained in [24]. According to [25],

$$a_\mu(\text{hadr}) = 6831(61)\times 10^{-11}, \quad a_\mu^{\text{exp}} - a_\mu^{\text{SM}} = 361(108)\times 10^{-11} \ [25]. \quad (12)$$

The $a_\mu^{\text{SM}}$ value is smaller by $3.3\sigma$ than the experimental value $a_\mu^{\text{exp}}$ obtained in [25]. Note that the analysis of the hadronic decay of the $\tau$ lepton reveals a $0.9\sigma$ discrepancy between $a_\mu^{\text{SM}}$ and $a_\mu^{\text{exp}}$.

The calculation provides the value

$$\delta\alpha_{\text{hadr}} = \frac{\alpha M_z^2}{3\pi}P\int\limits_{4m_\pi^2}^{\infty}\frac{R(s)ds}{(M_z^2-s)s} = 0.02786(6) \quad (13)$$

for the hadronic contribution to the electromagnetic coupling constant $\alpha(M_z)$. This result should be compared to the results $\delta\alpha_{\text{hadr}} = 0.02744(36)$ [26], 0.02803(65) [27], 0.02780(6) [2], 0.0280(7) [28], 0.02754(46) [29], 0.02784(22) [30], 0.02778(16) [31], 0.02779(20) [32], 0.02770(15) [33], 0.02787(32) [21], 0.02778(24) [35], and 0.02741(19) [36], which were obtained by calculating the integral in Eq. (13) with the experimental cross section for the $e^+e^-$ annihilation into hadrons.

We emphasize that the quantity $\delta\alpha_{\text{hadr}}$ is calculated here with the highest accuracy.

This work was supported by the Russian Foundation for Basic Research (project no. 00-02-17808), INTAS 2000 (grant no. 587), and the U.S. Civilian Research and Development Foundation for the Independent States of the Former Soviet Union (grant no. RP2-2247).

## REFERENCES

1. B. V. Geshkenbein and V. L. Morgunov, Phys. Lett. B **340**, 185 (1994).
2. B. V. Geshkenbein and V. L. Morgunov, Phys. Lett. B **352**, 456 (1995).
3. R. R. Akhmetshin, E. V. Anashkin, A. B. Arbuzov, *et al.*, Phys. Lett. B **527**, 161 (2002).
4. Particle Data Group, K. Hagiwara, K. Hikasa, K. Nakakura, *et al.*, Phys. Rev. D **66**, 010001-1 (2000).
5. B. V. Geshkenbeĭn, Yad. Fiz. **59**, 309 (1996) [Phys. At. Nucl. **59**, 289 (1996)].
6. B. V. Geshkenbein, hep-ph/0206094 v1; Phys. Rev. D **67**, 074006 (2002).
7. B. V. Geshkenbeĭn, Yad. Fiz. **51**, 1121 (1990) [Sov. J. Nucl. Phys. **51**, 719 (1990)].
8. B. V. Geshkenbeĭn and V. L. Morgunov, Yad. Fiz. **58**, 1873 (1995) [Phys. At. Nucl. **58**, 1771 (1995)].
9. M. A. Shifman, A. I. Vainstein, and V. I. Zakharov, Nucl. Phys. B **147**, 385 (1979).

10. B. V. Geshkenbeĭn, Yad. Fiz. **49**, 1138 (1989) [Sov. J. Nucl. Phys. **49**, 705 (1989)].
11. J. Bailey, J. K. Borer, F. Combley, *et al.*, Phys. Lett. B **68**, 191 (1977); F. J. M. Farley and E. Picasso, *Advanced Series on Directions in High Energy Physics*, Vol. 7: *Quantum Electrodynamics*, Ed. by T. Kinoshita (World Sci., Singapore, 1990).
12. R. M. Carey, W. Earle, E. Efstathiadis, *et al.*, Phys. Rev. Lett. **82**, 1632 (1999).
13. H. M. Brown, G. Bunce, R. M. Carey, *et al.*, Phys. Rev. D **62**, 091101 (2000).
14. H. N. Brown, G. Bunce, R. M. Carey, *et al.*, Phys. Rev. Lett. **86**, 2227 (2001).
15. G. W. Bennet, B. Bousquet, H. N. Brown, *et al.*, Phys. Rev. Lett. **89**, 101804 (2002); Err.: Phys. Rev. Lett. **89**, 129903 (2002).
16. V. W. Hughes and T. Kinoshita, Rev. Mod. Phys. **71**, s133 (1999).
17. A. Czarnecki and W. J. Marciano, Nucl. Phys. B (Proc. Suppl.) **76**, 245 (1999).
18. B. Krause, Phys. Lett. B **390**, 392 (1997).
19. R. Alemany, M. Davier, and A. Höcker, Eur. Phys. J. C **2**, 123 (1998).
20. M. Knecht and A. Nuffeler, Phys. Rev. D **65**, 073034 (2002).
21. M. Hayakawa and T. Kinoshita, Err.: Phys. Rev. D **66**, 019902 (2002); Err.: Phys. Rev. D **57**, 465 (1998).
22. J. Bijnens, E. Pallante, and J. Prades, Nucl. Phys. B **626**, 410 (2002).
23. A. Czarnencki, W. J. Marciano, and A. Vainshtein, hep-ph/0212229 (2002).
24. M. Davier, S. Eidelman, A. Höcker, and L. Zhang, hep-ph/0208177.
25. K. Hagiwara, A. D. Martin, Daisuke Nomura, and T. Teubner, hep-ph/0209187 v2.
26. A. D. Martin and D. Zeppenfeld, Phys. Lett. B **345**, 558 (1995).
27. S. Eidelman and F. Jegerlehner, Z. Phys. C **67**, 585 (1995).
28. H. Burkhardt and B. Pietrzyk, Phys. Lett. B **356**, 398 (1995).
29. M. L. Swartz, Phys. Rev. D **53**, 5268 (1996).
30. M. Davier and A. Höcker, Phys. Lett. B **419**, 419 (1998).
31. J. H. Kühn and M. Steinhauser, Phys. Lett. B **437**, 425 (1998).
32. J. Erler, Phys. Rev. D **59**, 054008 (1999).
33. M. Davier and A. Höcker, Phys. Lett. B **435**, 427 (1998).
34. S. Groote, J. G. Korner, K. Schilcer, and N. F. Nasrallah, Phys. Lett. B **440**, 375 (1998).
35. F. Jegerlehner, hep-ph/9901386.
36. A. D. Martin, J. Outhwaite, and M. G. Ryskin, Phys. Lett. B **422**, 69 (2000).

*Translated by R. Tyapaev*

JETP Letters, Vol. 77, No. 11, 2003, pp. 606–610. Translated from Pis'ma v Zhurnal Éksperimental'noĭ i Teoreticheskoĭ Fiziki, Vol. 77, No. 11, 2003, pp. 731–736.


# Destruction of a Solid Film under the Action of Ultrashort Laser Pulse

**S. I. Anisimov*, V. V. Zhakhovskiĭ**, ***, N. A. Inogamov*, K. Nishihara***, A. M. Oparin****, and Yu. V. Petrov***

**Landau Institute for Theoretical Physics, Russian Academy of Sciences, Chernogolovka, Moscow region, 142432 Russia*
***Institute of High Temperatures Scientific Association (IVTAN), Russian Academy of Sciences, Izhorskaya ul. 13/19, Moscow, 127412 Russia*
****Institute of Laser Engineering, Osaka University, Suita, Osaka 565-0871, Japan*
*****Institute of Design Automation, Russian Academy of Sciences, Moscow, 123056 Russia*
Received April 15, 2003

Molecular-dynamics (MD) simulation of the destruction of a crystal film heated by a femtosecond laser pulse was carried out. Heating is assumed to be instantaneous, because there is no time for the material to be displaced during the pulse. Film destruction is caused by the interaction of unloading waves. It can be considered as a model of a more complex process of splitting out of a thin surface layer from a massive target in the case where the layer remains solid after heating. It was found that the crystal order is broken due to the stretching strains and to the strong anisotropy of residual stress, resulting in a bipartition of the layer separating from the target. The lattice stretching and the formation of anisotropic stresses are due to the expansion of a heated lattice. © *2003 MAIK "Nauka/Interperiodica".*

PACS numbers: 61.80.Ba, 68.60.Dv; 79.20.Ds; 81.40.Vw

The use of ultrashort laser pulses opens up possibilities for improving the spatial resolution in surface processing (e.g., splitting off ultrathin layers or producing microreliefs on an irradiated surface) [1–7]. Another important application of ultrashort pulses is that the laser action splits off ultrathin layers from a solid body. After splitting off, these layers fly a distance of over several hundred of their thicknesses (several microns). Then they should separate into ultradispersed solid particles. These particles find various technological uses in sputtering [8], bombardment [9, 10], or analysis after the subsequent electrostatic acceleration [11, 12]. Apart from the applied aspects, the problem of laser-induced destruction of surface layers is of general physical interest.

The physical aspects of the action of ultrashort pulses on materials has been studied both experimentally and theoretically. In particular, optical methods were used to study a broad class of materials (metals, semiconductors, dielectrics) which can absorb laser pulses of a duration on the order of 100 fs [3, 4]. The ultrafast (during times comparable to the reciprocal Debye frequency) melt phenomenon was studied [13, 14]. The formation of the interference pattern (Newton fringes) was observed for all the studied metals and semiconductors in a certain range of light energy $Q$ (on the order of 0.1 J/cm$^2$) [3, 4]. This phenomenon is not observed for nanosecond and longer laser pulses, since the stress amplitudes are small, because the acoustic relaxation (the corresponding pressures are on the order of the saturation vapor pressures) and the ablation material runaway have mainly an evaporation character [1, 2, 8, 15, 16].

It was revealed in [17–19] that the interference fringes form due to splitting off of condensed material from the target. The ultrashort pulse energy is absorbed by the electron subsystem and transmitted to crystal lattice through electron–phonon relaxation within 10–100 ps [20–23]. The thickness $\delta$ of the heated layer near the crystal boundary with vacuum is equal either to the penetration depth of the electron heat wave within the electron–phonon relaxation time or to the skin layer depth, according to which of these values is greater [18, 19, 22]. At the hydrodynamic stage, a layer with thickness $\delta$ is split off. The calculations [18, 19, 22] and measurements of crater depth [3, 4] indicate that $\delta$ is on the order of 100 interatomic spacings. The molecular dynamic modeling is the most adequate method in this situation [19, 24, 25].

We now turn to the description of the problem and its solution. The heated layer expansion along the $x$ axis is modeled by the molecular-dynamics (MD) method with periodic boundary conditions for the transverse $y$ and $z$ coordinates. At zero time $t = 0$, the heated film occupies the region $-\delta < x < \delta$ and borders vacuum at the boundaries of this region. The MD calculations were carried out for the Lennard-Jones interatomic potential. At $t = 0$, atoms are packed into a face-centered cubic (fcc) lattice with the average density $n_0$ corresponding to the equilibrium state ($p = 0$) at tempera-

ture $T = 0$. The simulation amounts to the solution of the equations of motion for atoms and calculation of the macroscopic characteristics of the system. The simulation procedure is described in [19, 24, 25].

Figure 1 shows the phase diagram in $n$, $p_{xx}$ variables, where $p_{xx}$ is the longitudinal stress. For the temperatures considered $T < T_3$ ($T_3$ is the triple point temperature), the vapor pressure is exponentially small. For this reason, the binodal $b$ (condensed phase–vapor equilibrium curve) on the linear pressure scale virtually coincides with the straight line $p_{xx} = 0$. The curves $m_s$ and $m_f$ (Fig. 1) are the boundaries of a two-phase (liquid–solid body) melting region on the solid and liquid phases, respectively. The section *3*–*3*' corresponds to the triple point. After the absorption of laser energy, the substance undergoes transition from the initial state ($n_0$, $T = 0$, $p = 0$; fcc lattice; $A$ point in Fig. 1) to the state ($n_0$, $T_0$, $p_i$; $i$ point), which is the initial state for the subsequent hydrodynamic motion. The points corresponding to these initial states fill the isochore $n \equiv n_0$ ($p_{xx} \geq 0$). They are parameterized by the initial temperature $T_0$, which, in turn, is determined by the absorbed energy $Q$. At the point $i$, the pressure is isotropic: $p_{xx} = p_{yy} = p_{zz} = p_i$. We are interested in the crystal motion. Solid phase corresponds to the section of isochore $n_0$ above the melting curve $m_s$. At this section, the lattice symmetry (fcc) and constant $(4/n_0)^{1/3}$ are the same as for the cold crystal ($n_0$, $T = 0$).

Therefore, the instantaneous heating of the substance is described by the $A \longrightarrow i$ transition in the phase diagram (Fig. 1). The subsequent motion is isentropic. The substance expansion proceeds along the lower part of isentrope *1* (bsr) outgoing from point $i$ to lower densities. In the one-dimensional approximation, the expanding layer remains planar. This motion deforms the crystal only along the longitudinal axis $x$, while the atomic positions in the transverse directions $y$ and $z$ remain unchanged. The character of motion depends on the lattice orientation about the $x$ axis, along which the expansion occurs. Below, we consider the (110) orientation. In this case, the fcc crystal ($i$ point; $n = n_0$) deforms into a body-centered rhombohedral (bcr) crystal (curve *1*; $n < n_0$). The isentrope for an fcc crystal with constant $(4/n)^{1/3}$ ($n$ is the current density) corresponds to curve *2* (fcc). From the comparison of curves *1* and *2* in Fig. 1 it is seen that, for the uniaxial expansion, the pressure decreases faster than for the isotropic expansion. In points $S$ (intersection of the isentrope and spinodal), the magnitude of stress $p_{xx}$ is maximal. The curves drawn in Fig. 1 were obtained for the Debye model. They correspond well to other calculations [26–28], to the reference data on inert gases [29], and to the MD calculations presented below.

It has already been pointed out that Newton rings are observed only for a certain range of laser intensities $Q_d < Q < Q_u$. To explain this phenomenon, we note that there is a certain threshold in damaging the target. For

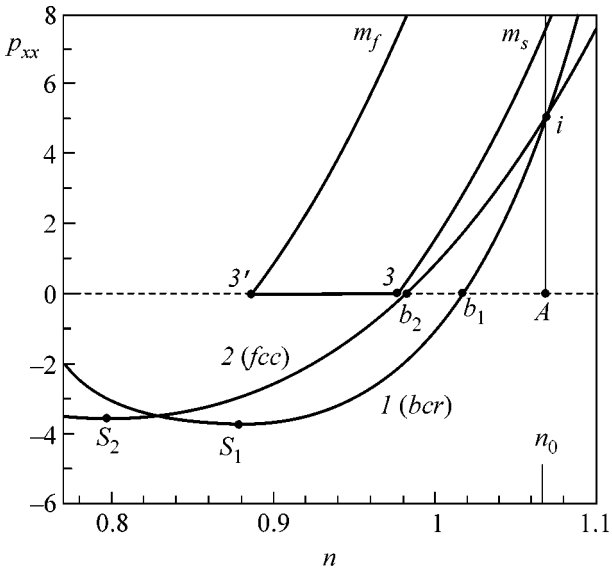


**Fig. 1.** Melting region $m_s$–$m_f$; section *3*–*3*' represents the triple point; isochore of initial states $A \longrightarrow i$; and above-threshold isentropes *1* (bcr) and *2* (fcc) ($T_0 = 0.8$). The points $b_j$, $S_j$ ($j = 1, 2$) correspond to the intersections of isentropes with binodal and spinodal. Numerical values are in units of Lennard-Jones potential.

laser intensities below a certain threshold, the surface layer does not split off, and Newton rings are not observed. As this threshold is overcome, a layer of thickness ~δ is split off, and the rings appear. Therefore, the lower boundary $Q_d$ of the intensity interval, for which the rings are observed, corresponds to the split-off threshold. The disappearance of the rings at the upper boundary $Q_u$ is explained by the fact that, as $Q$ increases, the thickness of the split-off condensed layer decreases (cf. [17–19]).

The split-off material is usually studied experimentally and semiempirically [30–35]. Ordinarily, the split-off process is analyzed for the shock-wave load. This situation differs from our fast (supersonic) heat load, because the shock wave compresses more and heats less. Accordingly, the threshold isentrope starting at the Hugoniot curve is farther from the melting region in the phase diagram than the isentrope starting at the isochore $n_0$. Whereas one can use Hooke's law, with a certain plasticity section, in studying the near-threshold shock destruction in the acoustic approximation (low temperatures [32–34]), heat load requires a phase-plane analysis. In this work, MD simulation of the thermal destruction upon an instantaneous heating was carried out. Note that our simulation is free of the semiempirical assumption about the destruction kinetics, and the number of atoms is equal, in the order of magnitude, to the atoms in the experiment.

The MD results are as follows. To describe the initial threshold temperature, a series of calculations with different $T_0$ values were carried out. It was shown that

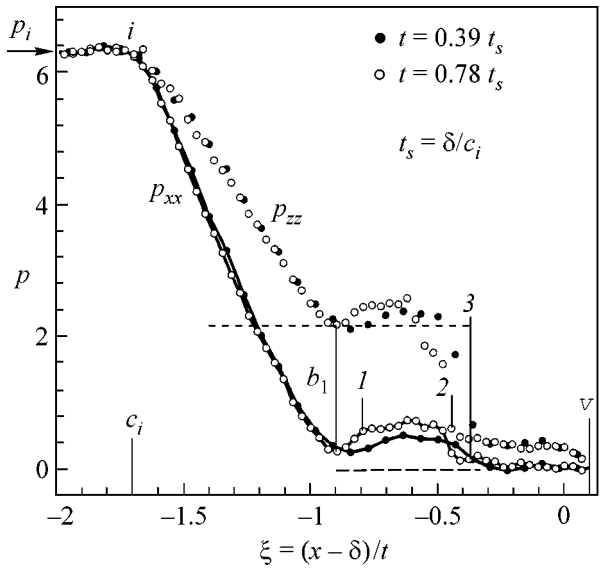


**Fig. 2.** Self-similar structure of the motion: rarefaction wave $i$–$b_1$; compression region *1–2*; plastic rarefaction wave *2–3* breaking crystal order; and the region of an approximately uniform flow *3*–$V$.

the destruction threshold corresponds to the temperature $T_0 = 0.75$. Hereafter, the quantities are given in MD units [19, 24, 25]. Isentropes *1* and *2* in Fig. 1 correspond to $T_0 = 0.8$, which is slightly above the destruction threshold. Let us consider this case in more detail. At the starting stage of moving from the boundary with vacuum, a self-similar rarefaction propagates, in which the profile is determined by the variable $\xi = (x - \delta)/t$. The wave consists of the section $i - b_1$ (Figs. 1, 2), where the pressure $p_{xx}$ decreases from its initial value to zero, and of the plateau $b_1 - V$, where the stream is constant and $p_{xx} = 0$ (dashed line in Fig. 2). The wave points $i$ and $b_1$ correspond to the $i$ and $b_1$ states (Fig. 1) in isotropic curve *1*. An important feature of the stream is the presence of a plastic rarefaction wave *2–3* (Fig. 2) where the fcc lattice is destroyed. Without this feature, the plateau would correspond to the trivial flow, for which the density $n$, the pressure $p$, and the velocity $U$ are constant.

Let us now discuss the stream structure and the reasons for the appearance of a plastic rarefaction wave. In liquid, the stresses $p_{jj}$ ($j = x, y, z$) are isotropic, so that the longitudinal and transverse stresses are zero in the $i$–$b_1$ wave and at plateau $b_1$–$V$. A different situation occurs in a solid state. Stresses $p_{jj}$ in initial state $i$ are isotropic. As the crystal expands, a stress anisotropy appears in the $i$–$b_1$ wave. As an example, Fig. 2 shows the dependences of $p_{xx}$ and $p_{zz}$ on $\xi$. The stresses $p_{jj}$ in the $i$–$b_1$ wave decrease because of the unit-cell deformation. This is also evidenced by both the Debye and MD computations.

The material is accelerated due only to the longitudinal component. In the $i$–$b_1$ wave, it is "unloaded" to zero (the bottom horizontal dashed section in the $p_{xx}(\xi)$ curve in Fig. 2). A bcr crystal undergoes the transition to the $b_1$ state (Fig. 1). The lattice in this crystal remains loaded in the transverse directions in the plateau region (the residual transverse stresses are shown by the upper dotted line in Fig. 2). The residual stresses are comparable to the initial pressure $p_i$ and make up 60% of $p_i$ in the $y$ (–110) direction and 35% in the $z$ (001) direction. The difference in the stresses is due to the inequivalence of the (–110) and (001) directions. As a result, a strongly anisotropic state forms at the plateau, for which the transverse-to-longitudinal stress ratio tends formally to infinity. The transverse stresses are precisely those which store the initial energy lattice compression, whose partial release in the bcr lattice destruction brings about the *2–3* wave.

Let us now analyze the dynamic effects caused by plastic wave *2–3*. In the expansion process, the material is thermally isolated, so that the change in the internal energy $E$ is caused by the work $\int pdV$. With the uniaxial stretching, pressure $p_{xx}$ decreases rapidly (cf. curves *1* and *2* in Fig. 1). Therefore, the energy $E_{fcc}(n)$ of the fcc lattice is lower (in isentrope *2*) than the energy $E_{bcr}(n)$ of the bcr lattice (in isentrope *1*). For the density $n_{b1}$ corresponding to the intersection of isentrope *1* and the binodal, the Debye calculation gives $\Delta E_{\max}(n_{b1}) = 0.071$ for the energy difference of the lattices. Since the energy $E_{fcc}$ corresponds to the equilibrium lattice (the lowest energy state), this is the maximum possible value.

The destruction of the bcr crystal is accompanied by energy release. In this case, the residual transverse stress decreases (Fig. 2), while the longitudinal stress slightly increases. Due to the increase in stress $p_{xx}$, the material is additionally stretched. Let us consider the influence of this effect on the flow character. The energy release $\Delta E$ increases the expansion velocity $U_{3V}$ in the region *3*–$V$ behind the plastic wave *2–3* ($U_{3V} > U_{12}$; Fig. 2) and increases the longitudinal pressure ($p_{12} > p_{3V} = 0$) in the region *1–2* ahead of wave *2–3*. Region *3*–$V$ terminates at the boundary with vacuum, so that the pressure $p_{xx}$ is zero ($p_{3V} = 0$). A two-wave structure arises (compression and rarefaction waves), because the region with enhanced pressure *1–2* propagates along the plateau with a longitudinal sound velocity that is higher than the plastic wave velocity.

We calculate this structure ignoring the width of transition region *2–3* (the density is assumed to decreases jumpwise). We write the mass, momentum, and energy conservation laws for the coupled jumps *1* and *2–3*. Ahead of the jump *1* (weak shock wave), the bcr lattice is in the state $b_1$ (density $n_{b1}$ and longitudinal pressure $p_{xx} = 0$). We use the system of coordinates related to the material in the state $b_1$. The parameters of


**Fig. 3.** Onset of the formation of the central $x = 0$ and peripheral $x = x_{add}$ fracture regions, $t = 2.3t_s$. The right half ($x > 0$) of the layer is shown. The label δ indicates the initial position of the boundary with vacuum.

uniform flow in the region *1–2* are determined from the pressure $p_{12}$: the velocity $u_{12} = -p_{12}/\rho_{b1}c_{b1}$, density excess (over $n_{b1}$) $\delta n_{12} = p_{12}/mc_{b1}^2$, and the velocity of jump *1* $c_{b1} + p_{12}/\rho_{b1}c_{b1}$, where $\rho_{b1} = n_{b1}m$, $m$ is the atomic mass, and $c_{b1}$ is the longitudinal sound velocity at the point $b_1$. Let $D$ be the velocity of wave *2–3* (as adopted, relative to the material ahead of jump *1*). From the mass and momentum balance equations for the jump *2–3*, we find the velocity of uniform flow in the region *3–v* $u_{3v} = (c_{b1} - D)p_{12}/\rho_{b1}c_{b1}D$ and a decrease in density $\delta n_{3v} = -(c_{b1} - D)^2 p_{12}/mc_{b1}^2 D^2$. Energy balance gives $p_{12}^2/\rho_{b1}^2 D^2 = 2\Delta E/m$.

These relations agree well with the MD calculation. Using the MD data on $p_{12}$ and $D$ and the above equation, we calculate the energy release $\Delta E$ in the plastic wave. It proves to make up 15% of the maximum possible $\Delta E_{\max}(n_{b1})$.

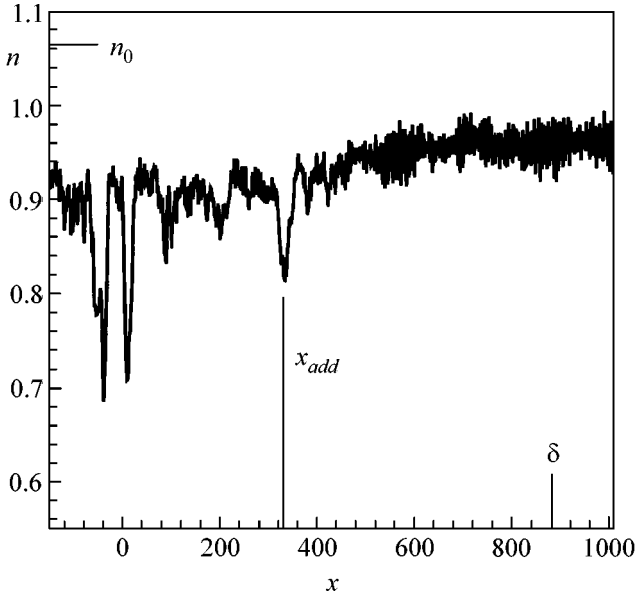


**Fig. 4.** Density profile after averaging over the transverse coordinates at $t = 2.32t_s$. The central fracture appears at $x \approx 0$. The position $x_{add}$ of the additional fracture and the initial position δ of the layer boundary with vacuum are shown.

The formation of two-wave structure has important consequences. In particular, it results in the appearance of two additional (apart from the central at $x = 0$) discontinuities lying symmetrically about the center at a considerable distance from it. Let us explain how this happens. Due to the increased pressure in region *1–2*, the second unloading step arises. At the first step, the pressure $p_{xx}$ decreases from $p_i$ to $p_{12}$, and at the second step it decreases from $p_{12}$ to zero. At the second step, the material is stretched substantially. A decrease in the density in wave *2–3* (Fig. 2) comprises 40% of the decrease in the primary wave $i \longrightarrow b_1$. A decrease in pressure at the first step $p_i \longrightarrow p_{12}$ is sufficient to break the crystal at the center $x = 0$. The excess of the initial temperature $T_0$ over the threshold $(T_0)_{thr}$ is small, so that the central fracture occurs at the time $t_{fr} \approx 1.8\delta/c_i$ when the characteristic $b_1$ appears at the center. The stress $p_{xx}$ is approximately constant along the characteristic $b_1$ reflected from the center. It is on the order of the limiting pressure at which the fracture happens. For this reason, when the reflected characteristic $b_1$ meets the plastic wave *2–3*, which additionally stretches the material, a new discontinuity appears (Fig. 3). The estimate for the position $x_{add}$ of this discontinuity gives $x_{add} \approx 0.3\delta$. The coordinates of the central and additional discontinuities correspond to the maxima at the density profile (Fig. 4). This profile is obtained by averaging with respect to the coordinates $y$ and $z$.

This work was supported by the Russian Foundation for Basic Research, project nos. 01-02-16136 and 02-02-17499. We are grateful to the Computational Center of the Osaka University and personally to Prof. S. Shimojo (Cybermedia Center, Osaka University) for the organization of large-scale computational experiments.

## REFERENCES

1. S. I. Anisimov, Ya. A. Imas, G. S. Romanov, and Yu. V. Khodyko, *Impact of High Power Radiation on Metals* (Nauka, Moscow, 1970).

2. S. I. Anisimov and B. S. Luk'yanchuk, Usp. Fiz. Nauk **172**, 301 (2002).
3. K. Sokolowski-Tinten, J. Bialkowski, A. Cavalleri, *et al.*, Phys. Rev. Lett. **81**, 224 (1998).
4. D. von der Linde and K. Sokolowski-Tinten, Appl. Surf. Sci. **154–155**, 1 (2000).
5. L. V. Zhigilei and B. J. Garrison, J. Appl. Phys. **88**, 1281 (2000).
6. F. Vidal, T. W. Johnston, S. Laville, *et al.*, Phys. Rev. Lett. **86**, 2573 (2001).
7. D. Perez and L. J. Lewis, Phys. Rev. Lett. **89**, 255504 (2002).
8. *Laser Ablation in Materials Processing: Fundamentals and Applications*, Ed. by B. Braren, J. J. Dubowski, and D. P. Norton; Mater. Res. Soc. Symp. Proc. **285** (1993).
9. R. J. Beuhler, J. Appl. Phys. **54**, 4118 (1983).
10. Sh. Akhunov, S. N. Morozov, and U. Kh. Rasulev, Nucl. Instrum. Methods Phys. Res. B (2003) (in press).
11. N. A. Inogamov, Pis'ma Zh. Tekh. Fiz. **10**, 769 (1984) [Sov. Tech. Phys. Lett. **10**, 323 (1984)].
12. A. I. Akishin, V. P. Kiryukhin, L. S. Novikov, *et al.*, Zh. Tekh. Fiz. **54** (1), 179 (1984) [Sov. Phys. Tech. Phys. **29**, 102 (1984)].
13. S. I. Ashitkov, M. B. Agranat, P. S. Kondratenko, *et al.*, Pis'ma Zh. Éksp. Teor. Fiz. **76**, 538 (2002) [JETP Lett. **76**, 461 (2002)].
14. B. Rethfeld, K. Sokolowski-Tinten, D. von der Linde, and S. I. Anisimov, Phys. Rev. B **65**, 092103 (2002).
15. N. M. Bulgakova and A. V. Bulgakov, Appl. Phys. A **73**, 199 (2001).
16. A. Miotello and R. Kelly, Appl. Phys. A (Suppl.) **69**, S67 (1999).
17. N. A. Inogamov, S. I. Anisimov, and B. Rethfeld, Zh. Éksp. Teor. Fiz. **115**, 2091 (1999) [JETP **88**, 1143 (1999)].
18. N. A. Inogamov, A. M. Oparin, Yu. V. Petrov, *et al.*, Pis'ma Zh. Éksp. Teor. Fiz. **69**, 284 (1999) [JETP Lett. **69**, 310 (1999)].
19. V. V. Zhakhovskiĭ, S. I. Anisimov, K. Nishikhara, and N. A. Inogamov, Pis'ma Zh. Éksp. Teor. Fiz. **71**, 241 (2000) [JETP Lett. **71**, 167 (2000)].
20. S. I. Anisimov, A. M. Bonch-Bruevich, M. A. El'yashevich, *et al.*, Zh. Tekh. Fiz. **36**, 1273 (1966) [Sov. Phys. Tech. Phys. **11**, 945 (1966)].
21. S. I. Anisimov, B. L. Kapeliovich, and T. L. Perel'man, Zh. Éksp. Teor. Fiz. **66**, 776 (1974) [Sov. Phys. JETP **39**, 375 (1974)].
22. S. I. Anisimov and B. Rethfeld, Proc. SPIE **3093**, 192 (1996).
23. B. Rethfeld, A. Kaiser, M. Vicanek, and G. Simon, Phys. Rev. B **65**, 214303 (2002).
24. V. V. Zhakhovskiĭ and S. I. Anisimov, Zh. Éksp. Teor. Fiz. **111**, 1328 (1997) [JETP **84**, 734 (1997)].
25. V. V. Zhakhovskii, S. V. Zybin, K. Nishihara, and S. I. Anisimov, Phys. Rev. Lett. **83**, 1175 (1999).
26. F. H. Ree, J. Chem. Phys. **73**, 5401 (1980).
27. Y. Choi, T. Ree, and F. H. Ree, J. Chem. Phys. **99**, 9917 (1993).
28. B. Smit, J. Chem. Phys. **96**, 8639 (1992).
29. V. A. Rabinovich, A. A. Vasserman, V. I. Nedostup, and L. S. Veksler, *Thermophysical Properties of Neon, Argon, Krypton, and Xenon* (Hemisphere, Berlin, 1998).
30. G. I. Kanel', S. V. Razorenov, A. V. Utkin, and V. E. Fortov, *Impact-Wave Phenomena in Condensed Media* (Yanus-K, Moscow, 1996).
31. S. I. Anisimov, A. V. Bushman, R. Z. Sagdeev, *et al.*, Pis'ma Zh. Éksp. Teor. Fiz. **39**, 9 (1984) [JETP Lett. **39**, 8 (1984)].
32. Kh. A. Rakhmatulin and Yu. A. Dem'yanov, *Solidity at Intensive Short-Time Loads* (Fizmatgiz, Moscow, 1961).
33. V. S. Nikiforovskiĭ and E. I. Shemyakin, *Dynamical Destruction of Solids* (Nauka, Novosibirsk, 1979).
34. N. Kh. Akhmadeev, *Dynamical Destruction of Solids in Stress Waves* (BNTs Ural. Otd. Akad. Nauk SSSR, Ufa, 1988).
35. V. N. Aptukov, P. K. Nikolaev, and A. A. Pozdeev, Dokl. Akad. Nauk SSSR **283**, 862 (1985) [Sov. Phys. Dokl. **30**, 705 (1985)].

*Translated by V. Sakun*

JETP Letters, Vol. 77, No. 11, 2003, pp. 611–615. Translated from Pis'ma v Zhurnal Éksperimental'noĭ i Teoreticheskoĭ Fiziki, Vol. 77, No. 11, 2003, pp. 737–742.


# Production of Powerful Electron Beams in Dense Gases

**V. F. Tarasenko[1, *], S. I. Yakovlenko[2, **], V. M. Orlovskiĭ[1], A. N. Tkachev[2], and S. A. Shunaĭlov[3]**

[1] *High Current Electronics Institute, Siberian Division, Russian Academy of Sciences, Akademicheskiĭ pr. 4, Tomsk, 634055 Russia*

**e-mail: VFT@loi.hcei.tsc.ru*

[2] *Institute of General Physics, Russian Academy of Sciences, ul. Vavilova 38, Moscow, 119991 Russia*

***e-mail: syakov@kapella.gpi.ru*

[3] *Institute of Electrophysics, Ural Division, Russian Academy of Sciences, ul. Komsomol'skaya 34, Yekaterinburg, 620049 Russia*

Received April 8, 2003; in final form, April 28, 2003

Subnanosecond electron beams with the record current amplitude (~70 A in air and ~200 A in helium) were produced at atmospheric pressure. The optimal generator open-circuit voltage was found for which the electron-beam current amplitude produced in a gas diode was maximal behind a foil. It was established that the electron beam was produced at the stage when the cathode plasma closely approaches the anode. It was shown that a high-current beam can be produced at high pressures because of the presence of the upper branches in the curves characterizing the electron-escape (runaway) criterion and the discharge-ignition criterion (Paschen curve). © *2003 MAIK "Nauka/Interperiodica"*.

PACS numbers: 52.80.Tn; 52.59.Mv; 84.30.Ng; 51.50.+v

## INTRODUCTION

The first communications on the detection of X-ray emission from pulsed discharges in dense gases appeared late in the 1960s [1, 2]. Later on, the formation of fast electrons and X-ray radiation in gas-filled diodes at elevated pressure was studied by a number of scientific groups [3, 4]. However, the amplitudes of electron-beam current did not exceed a few fractions of an ampere ($10^9$ electrons) in air at atmospheric pressure and several tens of amperes ($10^{12}$ electrons) in helium at a pressure of 22 torr [3]. It was shown in 2003 [5] that the electron-escape criterion has a basically nonlocal character in gas and corresponds to the situation where the electron-multiplication length (reciprocal Townsend coefficient [6]) becomes comparable to the interelectrode distance. Since the Townsend coefficient decreases at large $E/p$ values ($E$ is the electric-field strength and $p$ is the gas pressure), we deal with the upper branches of the curves characterizing the discharge-ignition criterion (Paschen curve) and the criterion for electron escape from the gap without multiplication. If the positions of the upper branches of these curves are known, one can determine the voltages at which the conditions for the electron escape are met for a given gas pressure and type and for a given interelectrode gap.

It is the purpose of this work to produce electron beams with the maximum possible amplitude in gas diodes at atmospheric pressure.

## EXPERIMENTAL SETUP

Our study was carried out using three different nanosecond pulse generators, which were described in detail in [7–9]. Generator 1 (SINUS) with a wave resistance of 30 Ω produced, on a matched load, a ~200-kV pulse with a duration of ~3 ns at its half-maximum and a duration of ~1 ns of its leading edge [7]. This generator was used with a diode filled with helium and air at a pressure of 760 torr and with two cathodes.

Cathode no. 1 was a set of three cylinders (with diameters 12, 22, and 30 mm) made from a 50-μm-thick titanium foil, which were inserted into each other and attached to a 36-mm-diameter duralumin substrate in such a way that they had a common axis. The ring height decreased by 2 mm on going from the smaller cylinder to the larger.

Cathode no. 2 was a 29-mm-diameter graphite pellet with the rounded edges and convex, with a radius of curvature of 10 cm, toward the foil. It was placed on a copper holder with a diameter of 30 mm. The design of the gas diode is shown in Fig. 1. The electron beam was extracted through a 45-μm-thick AlBe foil or through a 50% transparent grid. With this discharge-gap geometry, the electric field was enhanced near the cathode.

Generator 2 (RADAN-303) with a wave resistance of 45 Ω produced, on a matched load, voltage pulses from 50 to 170 kV (open-circuit voltage up to 340 kV) with a duration of ~5 ns at the pulse half-maximum and a duration of ~1 ns of the pulse leading edge [8]. The

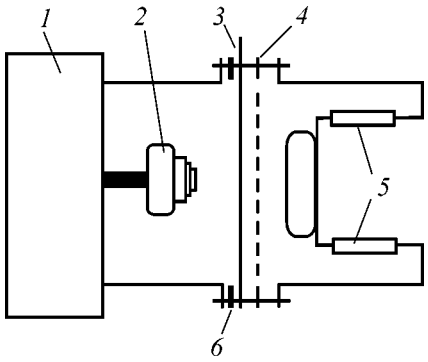


**Fig. 1.** Experimental setup: (*1*) generator, (*2*) cathode, (*3*) foil or grid, (*4*) additional foil for measuring beam-electron energy, (*5*) shunt for measuring beam current, and (*6*) shunt for measuring the total current in gas diode.

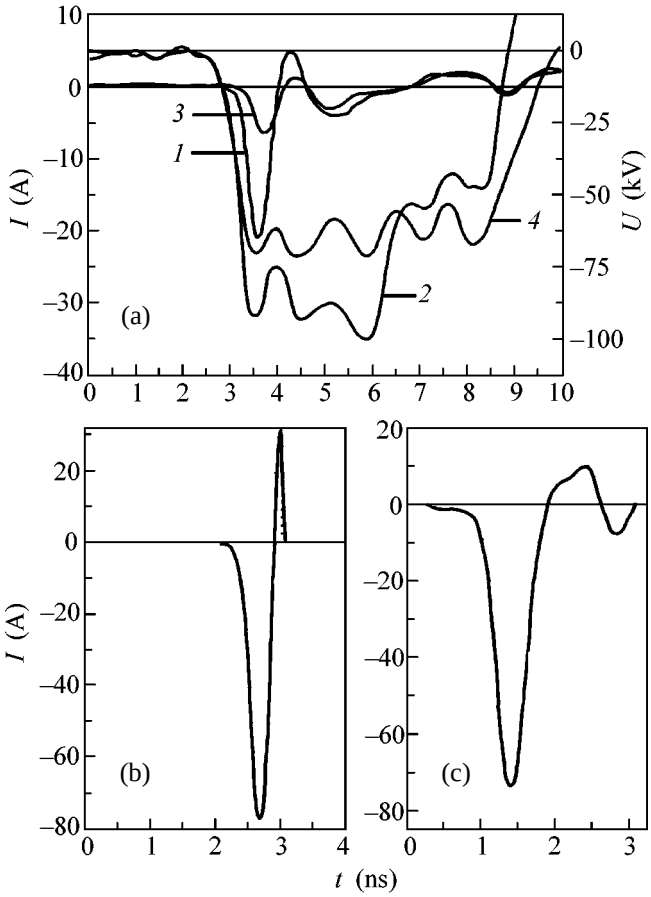


**Fig. 2.** (a) Oscillograms (*1*, *3*) of the current pulses behind a 45-μm-thick AlBe foil and (*2*, *4*) of the voltage pulses at the gas diode, as obtained with generator *2* in air at atmospheric pressure. The diode gap is $d$ = 16 mm and the generator open-circuit voltage is (*1*, *2*) 260 and (*3*, *4*) 155 kV. (b, c) Oscillograms of the electron-beam current behind a 45-μm-thick AlBe foil obtained with generator *3*. The diode gap is $d$ = 16 mm and the collector diameter is (b) 20 and (c) 50 mm.

bias on the gas space could be smoothly varied by changing the spark gap.

Generator 3 (RADAN-220) with a wave resistance of 20 Ω produced a voltage pulse with an amplitude of ~220 kV, a duration of ~2 ns at the pulse half-maximum, and a duration of ~0.3 ns of the pulse leading edge [9]. The design of the gas diode was the same for both RADAN generators and similar to that shown in Fig. 1. The flat anode, through which the electron beam escaped, was made from a 45-μm-thick AlBe foil. To extract the electron beam, 10-μm-thick aluminum foil or grids with a light transparency of 50–70% were also used. The cathode was a tube made from a 50-μm-thick steel foil with a diameter of 6 mm attached to a metallic rod of the same diameter. The distance between the cathode and anode varied from 13 to 20 mm.

The beam current was measured using a collector in the form of a copper disk with a diameter of 50 mm placed at a distance of 10 mm from the foil. The disk was connected to the accelerator body by a coaxial cable or, simultaneously, by a coaxial cable and a low-ohmic shunt. Small-area electrodes connected to the accelerator body by a coaxial cable, a graphite electrode connected to the accelerator body by a strip line, and the classical Faraday electrode were also used as a beam collector. The design of the Faraday cylinder allowed the gas to be pumped out by a backing pump from the space between the foil and the measuring electrode. The electron energy distribution was determined by the foil method. A TDS-684B oscillograph with a bandwidth of 1 GHz and 5 points per 1 ns was used to record the signals from the capacitor voltage divider, collector, and shunts. The recording system resolution was no worse than 0.3 ns. The discharge glow was photographed with a digital camera.

## RESULTS OF MEASUREMENTS

From the measurements of the gas-diode voltage pulses and the electron-beam current, as well as from the variation of the discharge shape upon changing the anode–cathode gap, cathode type, and gas-diode voltage, the following was established.

At atmospheric pressure of air in the gas diode, an electron beam with maximum current appears at the leading edge of the voltage pulse. It has a duration of no more than 0.4 ns at the half-maximum (Fig. 2). As the collector dimensions were reduced (to improve the time resolution), the beam-current pulse duration at the half-maximum was no more than 0.3 ns (Fig. 2b). It should be noted that, for the highest time resolution of the recording system, the durations of the leading and trailing current-pulse edges were different. The leading edge was smoother.

The positive pulse in the current oscillogram is caused by the unavoidable, though minimized, for the subnanosecond pulses, induction between the collector and the recording cable. With an increase in the collec-

tor size, the induction effect decreased, and the positive spike in the beam-current oscillogram decreased to ~10% (Fig. 2c). However, in this case, the time resolution was slightly impaired, and the duration of the current pulse behind the foil increased (by ~30%). For the highest beam currents, the pulse maximum was ordinarily observed immediately after the discharge-gap bias had reached its maximum. Under optimal conditions, the current-beam amplitude behind the foil was ~200 A at a gas pressure of 1 atm for generator 1 in helium and higher than 40 A in air for generator 1 and 70 A for generator 2 (Figs. 2b, 2c).

With an increase in the voltage amplitude, the beam-current maximum shifted to the onset of the voltage pulse and, for the maximum voltages, terminated at its leading edge, while the beam-current amplitude decreased under these conditions. As the open-circuit voltage decreased, the beam delay time increased to ~1 ns, and a beam appeared at the beginning of the quasistationary phase of the voltage pulse; however, the beam-current amplitude also noticeably decreased. Note that these trends were quite stable and were observed while extracting the electron beam through both the foil and the grid.

For a fixed interelectrode distance, duration of voltage-pulse front, and gas pressure and type (in a given particular case, 1 atm in air), there is a rather narrow voltage optimum in the generator no-load run, for which the amplitudes of the electron-beam current behind the foil are maximum (Fig. 3). We have observed the presence of this optimum. It should be noted that the gap-bias and discharge-current amplitudes depend on the open-circuit voltage of generator 2 almost linearly under the beam-generation conditions, inspite of the appreciable change in the beam-current amplitude (Fig. 3, curves *2, 3*). This strongly hampers the determination of the conditions under which the beam-current amplitude is maximal.

The discharge current appears with a short time delay after applying voltage to the gap and advances the electron-beam current behind the foil by 0.3–1 ns. The magnitude and duration of the discharge current appreciably exceed the beam-current amplitude and duration. For example, the amplitudes of discharge current and beam were, respectively, 2400 and 40 A in air for an open-circuit voltage of ~270 kV of generator 1 and a gap of 17 mm. After the beam-current pulse, the discharge ordinarily persisted at the quasistationary stage with a duration of few nanoseconds for a constant gap bias and had a volume character.

The photographs of plasma glow in the gas diode, as obtained from its end for the grid anode and from its side for the foil anode, are presented in Fig. 4. One can see that the discharge has the shape of volume jets, with the bright dots only at the cathode.

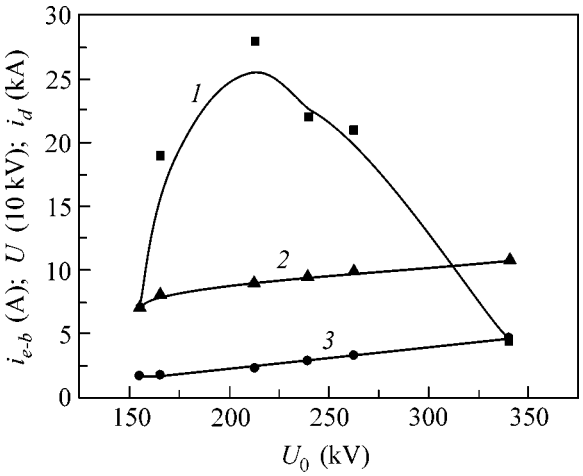


**Fig. 3.** The amplitudes (*1*) of the electron-beam current behind a 45-μm-thick AlBe foil, (*2*) of the bias on the gap, and (*3*) of the discharge current as functions of open-circuit voltage for generator *2*.

## INTERPRETATION OF THE RESULTS

In interpreting the beam formation process, we use the nonlocal criterion for the appearance of an appreciable number of electrons escaping the volume without multiplication, $\alpha_i d = 1$ [5]. Here, $\alpha_i$ is the Townsend coefficient and $d$ is the separation between the anode and cathode. We assume that the electron beam is formed at the instants of time when plasma approaches the anode.

Assuming $\alpha_i(E, p) = p\xi(E/p)$, where $\xi(E/p)$ is the function characteristic of the gas of interest, one can rewrite the criterion for the appearance of an appreciable number of electrons escaping the volume without multiplication, $\alpha_i(E_{cr}, p)d = 1$, in the form $pd\xi(U_{cr}/pd) = 1$. Here, $E_{cr} = U_{cr}/d$. This criterion determines a horseshoe-shaped curve $U_{cr}(pd)$ universal for the given gas, beyond which a considerable fraction of electrons escape the volume without multiplication (Fig. 5).

An important fact is that the $U_{cr}(pd)$ is an upper branch. This branch occurs because the Townsend coefficient decreases with increasing $E/p$. In turn, a decrease in the Townsend coefficient is caused by a decrease in the ionization cross section with increasing the energy of an incident electron and by the fact that the energy of multiplied electrons increases with $E/p$.

Note that one can hardly experimentally attain the values of $U$ and $pd$ for the upper branch, in particular, because of the influence of the cathode processes occurring at high electric field strengths [4]. To attain the upper branch in a dense gas, one must raise, rather rapidly, the electrode voltages and use electrodes, first of all a cathode, with a high plasma-formation threshold. Under our conditions, the voltage must be raised up to hundred kilovolt within a fraction of nanosecond.

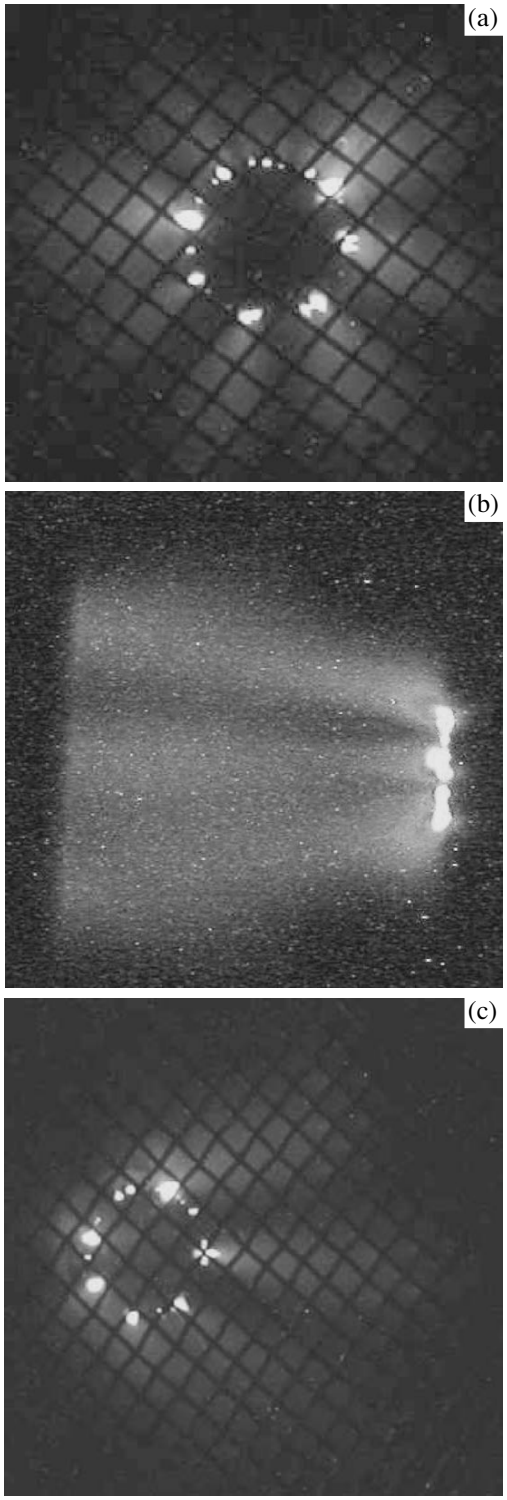


**Fig. 4.** The gap-discharge glow photographed (a) from the end, (b) from the side, and (c) at an angle. Generator 3 and a grid with a mesh with 1-mm sides.

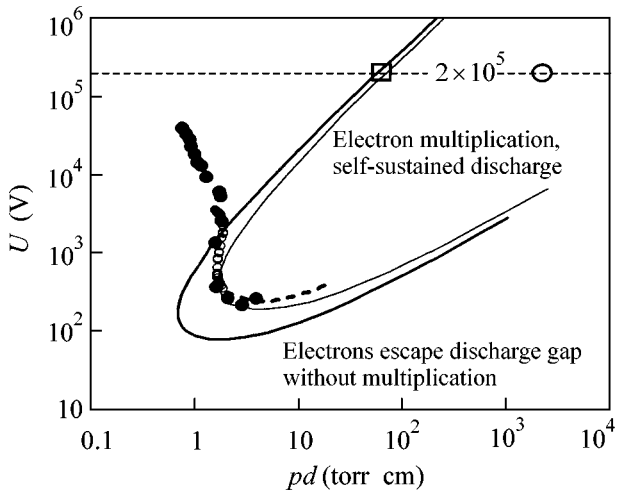


**Fig. 5.** (Solid thick line) the $U_{cr}(pd)$ function characterizing the electron escape criterion in helium, and (solid thin line $L = \ln(1 + 1/\gamma) = 2.45$) the $U_{br}(pd)$ function characterizing the discharge ignition criterion [5]. Light points are for the Penning experiment [10]; black points are the experimental results [11]; and the dashed line is for the experimental results from [6]. The large light circle at the top right corresponds to the maximal voltage obtained in our experiments at atmospheric pressure for the interelectrode separation $d$ = 28 mm. The large square corresponds to the situation where the "plasma cathode" approaches the anode at $d$ = 0.7 mm.

The function $U_{cr}(pd)$ is simply related to the ignition voltage $U_{br}(pd)$ of a self-sustained discharge. It is determined from the Townsend–Paschen condition $pd\xi(U_{br}/pd) = L \equiv \ln(1 + 1/\gamma)$ [6], where $\gamma$ is the coefficient of secondary electron emission and $U_{br}(pd) = LU_{cr}(pd/L)$. The function $U_{br}(pd)$ not only includes a portion of the familiar Paschen curve but also contains an additional upper branch discussed above. The $U_{cr}(pd)$ and $U_{br}(pd)$ curves obtained by numerical simulation for helium are shown in Fig. 5 together with the low-pressure experimental data [10, 11, 6]. Assuming $d$ = 28 mm, $U_{max}$ = 200 kV, and $p$ = 1 atm for the corresponding experimental conditions and uniform distribution of electric field in the gap (the latter assumption is rather crude for the gas diodes used), we obtain $pd = 2 \times 10^3$ torr cm. The corresponding point ($U_{max}$, $pd$) is drawn in Fig. 5 by a large circle. One can see that, to satisfy the electron-escape criterion, the $pd$ value should be approximately 30 times smaller than the experimental value. This contradiction cannot be eliminated by strengthening the cathode electric field. In addition, the electric field at the voltage pulse edge is much weaker than the maximal value. The electron escape criterion can be met at times when the plasma from cathode approaches anode. At $U_{max}$ = 200 kV and for uniform electric-field distribution in the gap, the escape criterion is met for $pd$ = 53 torr cm. For example, it is met for $d$ = 0.7 mm. This point is denoted in Fig. 5 by a large square.

For $U_{max}$ = 200 kV and $d$ = 0.7 mm, the ionization-wave velocity reaches $10^{10}$ cm/s. Correspondingly, the beam duration is $\tau \sim d/u \sim 10^{-2}$ ns. As was demonstrated

above (Fig. 2b), the beam duration does not exceed 0.3 ns at the half-maximum. It is quite possible that, after improving the time resolution, the beam-current pulse duration will be shorter and, accordingly, its amplitude will be larger.

The processes of plasma formation and ionization-wave propagation from cathode to anode are rather complicated and call for additional study. We will point out only the simplest positions. From the experimental data it follows that the ionization in the discharge gap is inhomogeneous and has the form of several jets (Fig. 4). The field at the end of the propagating plasma concentrates. As a result, the plasma propagation velocity may become comparatively high, so that the electron-escape criterion may be met (and the electron beam may form) at somewhat larger plasma-to-anode distances than in the planar geometry.

For example, if a bulge at the flat capacitor plate is shaped like a half of a prolate ellipsoid of revolution, the field magnification factor near the ellipsoid end is $k = 2\varepsilon^3(1-\varepsilon^2)^{-1}[\ln((1+\varepsilon)/(1-\varepsilon)) - 2\varepsilon]^{-1}$, where $a$ and $b$ are, respectively, the major and minor semiaxes and $\varepsilon = \sqrt{1-(b/a)^2}$ is the ellipsoid eccentricity [12]. For the semiaxes $a = 8$ mm and $b = 0.7$ mm, the field near the ellipsoid end is by $k = 36$ higher than the field between the capacitor plates and may reach $E/p \sim 1000$ V/(torr cm) at the middle of the gap. This field corresponds to ionization propagation velocity $u \sim 3 \times 10^9$ cm/s. For such a velocity, the generation of escaping electrons should start after approximately one nanosecond, as is the case in the experiment. Clearly, different jets may approach the anode at different times, thereby broadening the beam-current pulse.

Note also that the presence of a narrow maximum in the beam-current vs. generator open-circuit voltage curve (Fig. 3) is explained by the necessity of matching the instant of plasma approach to the anode and the maximum of interelectrode voltage.

## CONCLUSIONS

Subnanosecond electron beams with the record current amplitude (~70 A in air and ~200 A in helium) and electron energy (50–130 keV) were produced at atmospheric pressure in a gas diode. At a certain optimum of the generator open-circuit voltage the electron-beam current amplitudes behind the foil are maximal.

The assumption about the generation of electrons escaping at the instant of plasma approach to the anode allows the qualitative explanation of observed beam characteristics such as the generation delay and the short duration of the current pulse. An important fact is used that the curves have upper branches characterizing both the discharge ignition criterion (Paschen curve) and the criterion for electron escape from the gap without multiplication.

We are grateful to S.D. Korovin for providing us with the SINUS generator, to V.G. Shpak for providing us with the RADAN generator, and to V.G. Shpak, M.I. Yalandin, S.B. Alekseev, and A.V. Fedenev for assistance. This work was supported by the ISTC grant no. 1270.

## REFERENCES

1. Yu. É. Stankevich and V. G. Kalinin, Dokl. Akad. Nauk SSSR **177**, 72 (1967) [Sov. Phys. Dokl. **12**, 1042 (1967)].
2. R. C. Noggle, E. P. Kriger, and J. R. Wayland, J. Appl. Phys. **39**, 4746 (1968).
3. L. P. Babich, T. V. Loĭko, and V. A. Tsukerman, Usp. Fiz. Nauk **160**, 49 (1990) [Sov. Phys. Usp. **33**, 521 (1990)].
4. Yu. D. Korolev and G. A. Mesyats, *The Physics of Pulse Breakdown of Gases* (Nauka, Moscow, 1991).
5. A. N. Tkachev and S. I. Yakovlenko, Pis'ma Zh. Éksp. Teor. Fiz. **77**, 264 (2003) [JETP Lett. **77**, 221 (2003)].
6. Yu. P. Raĭzer, *The Physics of Gas Discharge* (Nauka, Moscow, 1992).
7. V. P. Gubanov, S. D. Korovin, I. V. Pegel', *et al.*, Izv. Vyssh. Uchebn. Zaved., Fiz., No. 12, 110 (1996).
8. M. I. Yalandin and V. G. Shpak, Prib. Tekh. Éksp., No. 3, 5 (2001).
9. F. Ya. Zagulov, A. S. Kotov, V. G. Shpak, *et al.*, Prib. Tekh. Éksp., No. 2, 146 (1989).
10. F. M. Penning, Physica (Amsterdam) **12**, 65 (1932).
11. A. N. Dikiji and B. N. Clarfeld, Zh. Tekh. Fiz. **25**, 1038 (1955).
12. V. V. Batygin and I. N. Toptygin, *Problems in Electrodynamics* (Fizmatgiz, Moscow, 1962; Academic, London, 1964).

*Translated by V. Sakun*

JETP Letters, Vol. 77, No. 11, 2003, pp. 616–618. Translated from Pis'ma v Zhurnal Éksperimental'noĭ i Teoreticheskoĭ Fiziki, Vol. 77, No. 11, 2003, pp. 743–746.


# Hall Conductivity of Minibands Lying at the Wings of Landau Levels

**J. Brüning[1], S. Yu. Dobrokhotov[2], V. A. Geyler[3,] *, and K. V. Pankrashkin[1,] ****

[1]*Faculty of Natural Sciences and Mathematics II, Humboldt-University of Berlin, Berlin, 12489 Germany*
[2]*Institute for Problems of Mechanics, Russian Academy of Sciences, pr. Vernadskogo 101, Moscow, 119526 Russia*
[3]*Laboratory of Mathematical Physics, Mordovian State University, ul. Bol'shevistskaya 68, Saransk, 430000 Russia*
**e-mail: geyler@mrsu.ru*
***e-mail: const@mathematik.hu-berlin.de*
Received May 5, 2003

A semiclassical method is suggested for the description of the energy spectrum of a two-dimensional magnetic Bloch electron in a periodic potential not necessarily smaller than the cyclotron energy. With this method, each Landau band is described as a spectrum of the appropriate one-dimensional Harper-type operator and represents a series of minibands, with the near-edge minibands being flat within the exponential accuracy. It is shown that, irrespective of the potential shape, all these minibands do not contribute to the quantized Hall conductivity.


PACS numbers: 73.43.Cd; 71.70.Di

In the standard theories of integer quantum Hall effect, each filled Landau level makes a contribution of quantum $e^2/h$ to the Hall conductivity [1], so that, as the Fermi level rises, the Hall conductivity monotonically increases with the $e^2/h$ jumps that were discovered experimentally by K. von Klitzing. In a weak periodic potential $V$, each Landau level spreads into a band with a width no greater than $2\max|V|$; each band, in turn, is split into magnetic subbands. If the number of magnetic-flux quanta $\Phi_0 = hc/|e|$ of the magnetic flux $\Phi$ through the unit cell of the periodic potential $V$ is rational and can be represented as a noncancelable fraction $\Phi/\Phi_0 = N/M$, each of the Landau bands splits into $N$ subbands [2]. As a result, the "flux–energy" diagram for the spectrum of Landau periodic operator assumes a complex fractal structure that was predicted by Azbel and constructed numerically in the approximation of Harper equation [3] (Hofstadter's butterfly). From the well-known gauge arguments of R. Laughlin, it follows that each subband has an integer number of conductivity quanta, which changes in a rather irregular way upon the transition from one subband to the other and obeys a certain Diophantine equation [1] (this number exactly equals the Chern number for the corresponding vector bundle of the Bloch magnetic functions [4]). Therefore, in the presence of a periodic potential in the fields where $\Phi/\Phi_0$ is on the order of unity, the dependence of Hall conductivity on the Fermi energy becomes nonmonotonic and, generally, exhibits irregular jumps, again with the magnitudes being multiples of $e^2/h$. These jumps have recently been observed by K. von Klitzing *et al.* in [5] (in full agreement with the predictions of theory [1]) in measuring the magnetoresistance of a two-dimensional electron gas in a square superlattice with a ~100-nm unit cell. It should be noted that the idea of that experiment was suggested as early as in [3].

Inasmach as $V$ in [5] was $\simeq$0.6 meV, the superposition or partial overlap of the Landau bands did not need to be taken into account in that work. However, this effect cannot be neglected for the larger potential $V$. As was shown numerically in [6], if $V$ becomes comparable to the cyclotron energy $\hbar\omega_c$, the Landau bands overlap and are even rearranged upon further increase in $V$. It is significant that, after the crossover, the Chern number for several lower-lying bands is zero; i.e., these bands do not contribute to the Hall conductivity [6]. A more detailed numerical analysis of the influence of the overlap between the Landau bands on the Hall resistivity was carried out in [7]. It should be taken into account that the flux–energy diagram for a periodic Landau operator is different from the ideal self-similar Hofstadter butterfly [8]. The subband Hall conductivity is also affected by the form of the potential curve, in particular, by the presence or absence of the center of inversion [9].

In this work, we propose a semiclassical approach to the Landau bands that is independent of the potential shape and the band overlap. Only two parameters are assumed to be small: $\varepsilon_B = (l_M/L)^2$, where $l_M$ is the magnetic length and $L$ is the characteristic size of the lattice period of potential $V$, and the value of the parameter $\varepsilon_V = \varepsilon_B\max|V|/\hbar\omega_c$. The ratio $\max|V|/\hbar\omega_c$ should not necessarily be small, so that our approach also applies to the regime of Landau band rearrangement [6]. In the

typical situations, the estimates for the parameters $\varepsilon_B$ and $\varepsilon_V$ are as follows: if $B \simeq 10$ T then $l_M \simeq 10$ nm; for the periodical quantum-dot or quantum-antidot arrays, $L \simeq$ 100–500 nm. Hence, $\varepsilon_B \sim 10^{-3}$; for the electron effective mass in GaAs $m = 0.067m_e$, one gets $\hbar\omega_c \simeq$ 15 meV. For this reason, one has $\varepsilon_V \lesssim \varepsilon_B$ for $V \lesssim 15$ meV. Within this approach, we demonstrate that, irrespective of the form of the potential curve, all minibands lying at the wings of Landau levels (and not only the lowest lying subbands) make no contribution to the Hall conductivity. Thus, when describing the influence of the overlap of Landau bands on the quantization of Hall conductivity, one should take into account only the overlap between rather narrow central regions of the smeared Landau levels.

The Hamiltonian of a Bloch magnetic electron in the Landau gauge has the form

$$\hat{H} = \frac{\hbar^2}{2m}((-i\partial_1 + (eB/c\hbar)x_2)^2 - \partial_2^2) + V(x_1, x_2),$$

where the potential $V$ has a lattice with periods and the basis $\mathbf{a}_1 = (L, 0)$ and $\mathbf{a}_2$. In the dimensionless coordinates $\mathbf{X} = \mathbf{x}/L$ and potential $v = V/\max|V|$, $\hat{H}$ is written as $\hat{H} = mL^2\omega_c^2\hat{H}^0$, where

$$\hat{H}^0 = \frac{1}{2}[(\hat{P}_1 + X_{2s})^2 + \hat{P}_2^2] + \varepsilon_V v(X_1, X_2).$$

Here, $\hat{P}_j = -i\varepsilon_B\partial/\partial X_j$.

The perturbation theory with respect to the small parameter $\varepsilon_V$ can provide only crude information; moreover, it requires additional assumptions about the relationship between $\varepsilon_B$ and $\varepsilon_V$, because the parameter $\varepsilon_B$ is small. Nevertheless, the smallness of $\varepsilon_B$ allows the fine structure of Landau levels to be described semiclassically.

Since the classical trajectories in the $(X_1, X_2)$ plane for the unperturbed Hamiltonian $\frac{1}{2}((P_1 + X_2)^2 + P_2^2)$ are cyclotron orbits with radii $\sqrt{2I}$ centered at $(y_1, y_2)$, one can pass on to the new canonical variables, namely, to the generalized momenta $I, y_1$ (or $p, y_1$) and generalized positions $\varphi, y_2$ (or $q, y_2$), according to the formulas

$$X_1 = q + y_1, \quad P_1 = -y_2, \quad X_2 = p + y_2,$$
$$P_2 = -q, \quad p = \sqrt{2I}\cos\varphi, \quad q = \sqrt{2I}\sin\varphi$$

($\varphi$ is the orbital angular coordinate). In these variables, the corresponding classical Hamiltonian $H^0$ is

$$H^0 = I + \varepsilon_V v(\sqrt{2I}\sin\varphi + y_1, \sqrt{2I}\cos\varphi + y_2).$$

After angular averaging of $H_0$, the drift of the center of the cyclotron orbit is described by the averaged Hamiltonian

$$\mathcal{H}^{\text{av}}(I, y_1, y_2; \varepsilon_V) = \frac{1}{2\pi}\int_0^{2\pi} H^0 d\varphi$$
$$= I + \varepsilon_V J_0(\sqrt{-2I\Delta})v(y_1, y_2),$$
$$\Delta = \frac{\partial^2}{\partial y_1^2} + \frac{\partial^2}{\partial y_2^2}$$

($J_0$ is the zero-order Bessel function). One can also show that there is a canonical variable change $(p', q', \mathbf{y}') = (p, q, \mathbf{y}) + O(\varepsilon_V)$ such that

$$H^0(p, q, \mathbf{y}; \varepsilon_V) = \mathcal{H}^{\text{av}}\left(\frac{1}{2}(p'^2 + q'^2), \mathbf{y}'; \varepsilon_V\right) + O(\varepsilon_V^2),$$

but the estimate of the residue $O(\varepsilon_V^2)$ in this formula does not suffice to describe the $H^0$ fine structure. However, it was shown in [10], that this procedure can be iterated up to the canonical change of the variables $(P, Q, \mathbf{Y}) = (p, q, \mathbf{y}) + O(\varepsilon_V)$, to bring the $H^0$ Hamiltonian to the form $H^0(p, q, \mathbf{y}; \varepsilon_V) = \mathcal{H}^0\left(\frac{1}{2}(P^2 + Q^2), Y_1, Y_2; \varepsilon_V\right) + O(e^{-C/\varepsilon_V})$, with the right-hand side periodic in the variable $Y_j$ and with a positive constant $C$.

The quantization of $\mathcal{H}^0$ brings about the $\hat{\mathcal{H}}^0$ operator, whose semiclassical spectrum coincides with that of $\hat{H}^0$ and $\hat{\mathcal{H}}^0$ to an accuracy of $O((\varepsilon_B + \varepsilon_V)^\nu)$ for an arbitrary $\nu$. Since the operators $\hat{P} = -i\varepsilon_B\partial/\partial Q$ and $\hat{Q} = Q$ commute with $\hat{Y}_1 = -i\varepsilon_B\partial/\partial Y_2$ and $\hat{Y}_2 = Y_2$, $\hat{\mathcal{H}}^0$ commutes with the Hamiltonian of harmonic oscillator $\frac{1}{2}(\hat{P}^2 + \hat{Q}^2)$. Therefore, the eigenfunctions $\Psi$ of the operator $\hat{\mathcal{H}}^0$ can be sought in the form $\Psi(Q, Y_2) = \psi_n(Q)\varphi_n(Y_2)$, where $\psi_n$ are the oscillator functions for the $E_n = (n + 1/2)\varepsilon_B$ level ($n = 0, 1, 2, \ldots$) and $\varphi_n$ satisfy the equation

$$\hat{\mathcal{H}}_n\varphi_n = E\varphi_n. \quad (1)$$

Here, $\hat{\mathcal{H}}_n$ are found from the classical Hamiltonian $\mathcal{H}_n(Y_1, Y_2) = \mathcal{H}^0(E_n, Y_1, Y_2, \varepsilon_V)$ by the quantization $\hat{Y}_1 = -i\varepsilon_B\partial/\partial Y_2$ (these operators are conventionally called the Harper-type operators). Since $mL^2\omega_c^2\varepsilon_B = \hbar\omega_c$, $E_n$ is exactly the $n$th Landau level. Hence, the spectrum of operator $\hat{\mathcal{H}}_n$ describes the spreading of the $n$th Landau level into band under the action of the periodic potential $V$.

Therefore, each Landau band in our approach is described by Eq. (1), and the initial spectral problem reduces to the family of one-dimensional spectral problems, allowing the problem to be integrated.

Let us now use the analysis of Harper operators [11]. At the edges of the spectrum of operator $\hat{\mathcal{H}}_n$, there are minibands with widths exponentially small in the parameter $\varepsilon_B$. The corresponding Bloch magnetic eigenfunctions of the operator $\hat{H}^0$ for the rational flux $\Phi/\Phi_0$ are constructed in [10]. Namely, by denoting $\Phi/\Phi_0 = N/M$ and enlarging the lattice $\Lambda$ (i.e., going to the lattice with basis $M\mathbf{a}_1$ and $\mathbf{a}_2$ [4]), one has the following semiclassical eigenfunctions in the $\mathbf{X}$ coordinates satisfying the magneto-Bloch periodic conditions with the quasimomentum $\mathbf{k}$:

$$\Psi(\mathbf{X}, \mathbf{k}) = \sum_{l_1, l_2 \in \mathbb{Z}} e^{2\pi i(k_1 l_1 - k_2 l_2) - iNl_2 L_{21}/2} \times \psi(\mathbf{X} - Ml_1\mathbf{L}_1 - l_2\mathbf{L}_2) e^{-iNl_2 X_1}, \quad (2)$$

where $\mathbf{L}_1 = (1, 0)$ and $\mathbf{L}_2 = (L_{21}, L_{22})$ are the periods of the normalized potential $v$ and $\psi$ is a certain localized function quasimode of the $\hat{H}$ operator [12]. From Eq. (2) it directly follows that the vector bundle of the Bloch magnetic functions for the exponentially narrow miniband is trivial and, therefore, has the zero Chern class. According to the standard theory of the Hall quantum effect [1], this means that the Hall conductivity for this miniband is zero. Thus, after the Fermi level crosses the minibands, the quantized Hall conductivity at the Landau level wings does not change. As to the minibands in the middle of Landau bands, the corresponding contribution to the Hall conductivity requires additional calculations, which can conveniently be performed using the Usov formulas [13]. The calculations of this type depend on the particular form of the potential $V$ and have been carried out, e.g., in [9]. The simplest examples indicate that the dependence on the Fermi level is nonmonotonic, in accordance with [1].

In summary, a semiclassical approach is proposed to reduce the description of the Bloch magnetic electron spectrum to a series of one-dimensional problems. With this approach, each Landau band (smeared Landau level) coincides with the spectrum of some one-dimensional Harper-type operator obtained by the quantization of a classical Hamiltonian on the torus for a given level. At the wings of Landau bands, there are exponentially narrow minibands, and the vector bundle of the corresponding semiclassical Block magnetic functions has the zero Chern class. Therefore, these minibands do not contribute to the quantized Hall conductivity, and they can be neglected when considering the influence of overlap of Landau bands on the Hall quantization pattern. It is significant that the method described in this work applies when the lattice potential $V$ is comparable to the cyclotron energy; if $|V| \ll \hbar\omega_c$, our results agree with [14]. Interestingly, the structure of layering of the Bloch magnetic functions for the exponentially narrow (i.e., flat, to the exponentially small field corrections) minibands is the same as for the layering of the fermion eigenfunctions for a lattice in the presence of a magnetic field [15].

This work was supported by the Russian Foundation for Basic Research, INTAS, and DFG.

## REFERENCES

1. D. J. Thouless, M. Kohmoto, M. P. Nightingale, and M. den Nijs, Phys. Rev. Lett. **49**, 405 (1982); P. Streda, J. Phys. C **15**, L717 (1982).
2. J. Zak, Phys. Rev. **134**, A1602 (1964).
3. M. Ya. Azbel', Zh. Éksp. Teor. Fiz. **46**, 929 (1964) [Sov. Phys. JETP **19**, 634 (1964)]; D. R. Hofstadter, Phys. Rev. B **14**, 2239 (1976).
4. B. A. Dubrovin and S. P. Novikov, Zh. Éksp. Teor. Fiz. **79**, 1006 (1980) [Sov. Phys. JETP **52**, 511 (1980)].
5. C. Albrecht, J. H. Smet, K. von Klitzing, *et al.*, Phys. Rev. Lett. **86**, 147 (2001).
6. Z. Tešanović, F. Axel, and B. I. Halperin, Phys. Rev. B **39**, 8525 (1989).
7. D. Springsguth, R. Ketzmerick, and T. Geisel, Phys. Rev. B **56**, 2036 (1997).
8. G. Petschel and T. Geisel, Phys. Rev. Lett. **71**, 239 (1993); O. Kühn, V. Fessatidis, H. L. Cui, *et al.*, Phys. Rev. B **47**, 13019 (1993); S. A. Gredeskul, M. Zusman, Y. Avishai, and M. Ya. Azbel, Phys. Rep. **288**, 223 (1997); V. A. Geyler, I. Yu. Popov, A. V. Popov, and A. A. Ovechkina, Chaos, Solitons, and Fractals **26**, 251 (2000).
9. V. Ya. Demikhovskiĭ and A. A. Perov, Pis'ma Zh. Éksp. Teor. Fiz. **76**, 723 (2002) [JETP Lett. **76**, 620 (2002)]; V. Ya. Demikhovskii and D. V. Khomitsky, Phys. Rev. B **67**, 035321 (2003).
10. J. Brüning and S. Yu. Dobrokhotov, Dokl. Akad. Nauk **379**, 131 (2001); J. Brüning, S. Yu. Dobrokhotov, and K. V. Pankrashkin, Russ. J. Math. Phys. **9**, 14 (2002); Teor. Mat. Fiz. **131**, 304 (2002).
11. F. Faure, J. Phys. A **33**, 531 (2000).
12. V. P. Maslov and M. V. Fedoryuk, *Semi-Classical Approximation in Quantum Mechanics* (Nauka, Moscow, 1976; Reidel, Dordrecht, 1981).
13. N. A. Usov, Zh. Éksp. Teor. Fiz. **94** (12), 305 (1988) [Sov. Phys. JETP **67**, 2565 (1988)].
14. G. V. Mil'nikov and I. M. Sokolov, Pis'ma Zh. Éksp. Teor. Fiz. **48**, 494 (1988) [JETP Lett. **48**, 536 (1988)].
15. A. F. Belov, Yu. E. Lozovik, and V. A. Mandel'shtam, Pis'ma Zh. Éksp. Teor. Fiz. **51**, 422 (1990) [JETP Lett. **51**, 481 (1990)]; Y. Hatsugai, M. Kohmoto, and Y.-S. Wu, Phys. Rev. Lett. **73**, 1134 (1994); V. A. Geĭler and I. Yu. Popov, Pis'ma Zh. Éksp. Teor. Fiz. **63**, 367 (1996) [JETP Lett. **63**, 381 (1996)].

*Translated by V. Sakun*

JETP Letters, Vol. 77, No. 11, 2003, pp. 619–624. Translated from Pis'ma v Zhurnal Éksperimental'noĭ i Teoreticheskoĭ Fiziki, Vol. 77, No. 11, 2003, pp. 747–752.


# Electronic and Structural Transitions in $NdFeO_3$ Orthoferrite under High Pressures

**A. G. Gavriliuk[1], I. A. Troyan[1], R. Boehler[2], M. I. Eremets[2], I. S. Lyubutin[3], and N. R. Serebryanaya[4]**

[1] *Institute of High Pressure Physics, Russian Academy of Sciences, Troitsk, Moscow region, 142190 Russia*
[2] *Max-Planck Institut fur Chemie, 55020 Mainz, Germany*
[3] *Shubnikov Institute of Crystallography, Russian Academy of Sciences, Moscow, 119333 Russia*
*e-mail: lyubutin@ns.crys.ras.ru*
[4] *Institute of Superhard and Novel Carbon-Base Materials, Troitsk, Moscow region, 142190 Russia*

Received May 5, 2003

The effect of high pressure up to 65 GPa on the crystal structure and optical absorption spectra of $NdFeO_3$ orthoferrite single crystals is studied in diamond anvil cells. At $P \sim 37.5$ GPa, an electronic transition at which the optical absorption edge jumps from ~2.2 to ~0.75 eV is observed. The equation of state $V(P)$ is studied on the basis of the *X*-ray diffraction data obtained under pressure. This study reveals a first-order structural phase transition at $P \sim 37$ GPa with a jump of ~4% in the unit cell volume. It is shown that the phase transition observed in rare-earth orthoferrites at 30–40 GPa is a transition of the insulator-to-semiconductor type. © *2003 MAIK "Nauka/Interperiodica".*

PACS numbers: 61.50.Ks; 62.50.+p; 64.70.Kb; 78.40.Kc

## 1. INTRODUCTION

The orthorhombic orthoferrites $RFeO_3$, where *R* is a rare-earth element, crystallize as $CaTiO_3$ perovskite-type structures, in which *R* occupies the Ca sites and Fe occupies the Ti sites. The space group of orthoferrites is *Pbnm* [1, 2]. All $Fe^{3+}$ ions are crystallographically equivalent and have an octahedral oxygen environment. A change in *R* leads to a orthorhombic distortion, which almost does not affect the oxygen octahedra around the iron ions but tilts the octahedron axis off the *c* axis and, hence, changes the Fe–O–Fe valence bond angle [3]. The mean values of the Fe–O and O–O interatomic distances are practically constant for the whole $RFeO_3$ rare-earth series and make 2.011 and 2.844 Å, respectively [2]. The deviation from the cubic symmetry grows as the $R^{3+}$ ion radius decreases (a chemical compression), so that this deviation is minimal in $LaFeO_3$ and maximal in $LuFeO_3$.

The magnetic structure of an orthoferrite is such that each iron ion is surrounded by six $Fe^{3+}$ ions, and the Fe–O–Fe superexchange angle is within $157° > \varphi > 142°$ (for *R* varying from La to Lu) [3]. As a result of the $Fe^{3+}$–$O^{2-}$–$Fe^{3+}$ strong negative exchange interaction, two magnetic sublattices are formed with almost antiparallel moments. The small angle between the magnetic moments of the iron sublattices gives rise to a weak ferromagnetic moment [4, 5]. The magnetic moments of the *R* ions are ordered only at very low temperatures, while at $T > 10$ K they do not affect the basic magnetic properties of orthoferrites.

In our recent studies of the effect of high pressure on both the Néel temperature $T_N$ and the hyperfine magnetic fields on nuclei in $NdFeO_3$ and $LuFeO_3$ orthoferrites [6], we separated the radial and angular contributions to the Fe–O–Fe exchange interaction and the hyperfine interaction and estimated their magnitudes and signs. The X-ray studies of a $LuFeO_3$ single crystal [7] showed that, as the pressure *P* increases, all three parameters, *a*, *b*, and *c*, of the unit cell decrease, and, under the pressures $P > 30$ GPa, the parameters *a* and *b* become equal, which presumably testifies to a transition to the tetragonal phase [8]. In addition, for $LuFeO_3$ in the same pressure range, we observed an electron transition accompanied by a drop in the optical absorption edge from ~ 2.2 to ~ 1.2 eV [9].

Recently, for $LaFeO_3$ orthoferrite, Hearne with coauthors [10] revealed a transition from magnetic to nonmagnetic state (at room temperature) at approximately the same pressures. It was interpreted as the transition of the $Fe^{3+}$ ions from the high-spin state $S = 5/2$ to the low-spin state $S = 1/2$ (spin crossover).

In this paper, we study the structure and the optical absorption spectra of a $NdFeO_3$ single crystal under high pressures up to 65 GPa obtained in diamond anvils. At $P \sim 37.5$ GPa, we observed an electronic transition with a drop in the optical absorption edge from ~2.2 to ~0.7 eV. This drop testifies to an insulator-to-semiconductor transition. In the same pressure interval, we observed a first-order structural phase transition with a drop of about 4% in the unit-cell volume.

0021-3640/03/7711-0619$24.00 

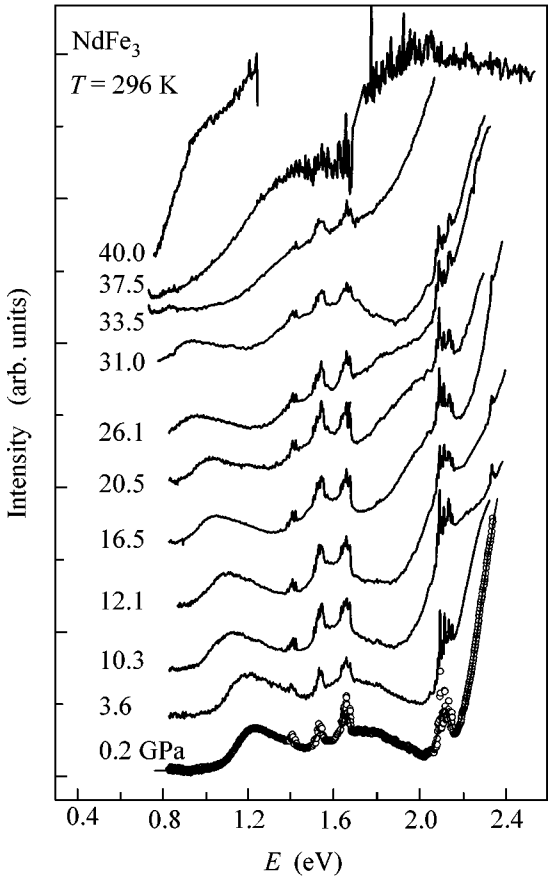


**Fig. 1.** Optical absorption spectra of a $NdFeO_3$ single crystal at room temperature under different pressures. The dots represent experimental points, and the solid lines display the nonlinear approximation (see text).

## 2. EXPERIMENTAL TECHNIQUE

High-quality $NdFeO_3$ single crystals were grown by the hydrothermal method at the Shubnikov Institute of Crystallography of the Russian Academy of Sciences. The effect of high pressures up to 40 GPa on the optical absorption spectra of $NdFeO_3$ orthoferrite was studied in a diamond anvil cell at room temperature. The diamond anvils were about 400 μm in diameter. The diameter of the hole at the center of the rhenium gasket was about 120 μm. The sample used for the measurements was a plate with the dimensions $\sim 50 \times 50 \times 10$ μm. The plate was split from a bulk $NdFeO_3$ single crystal. The orientation of the plate was not identified. The pressure-transmitting medium was polyethyl siloxane liquid (PES-5), which provided a quasi-hydrostatic compression. After the pressure was relieved, single crystal remained undestroyed. The optical system used for studying the absorption spectra under high pressure allowed the measurements in the visible and near-infrared ranges (from 0.3 to 5 μm). The experimental setup used mirror optics for focusing the light beam on the sample and also for focusing the transmitted radiation onto the entrance slit of an optical monochromator. In this way, it was possible to avoid chromatic aberration. In the visible range, the role of the detector was played by a photomultiplier (FEU-100), and in the near-infrared region, the light was detected by a germanium diode mounted on a cold finger, which was cooled by liquid nitrogen. The diameter of the light spot on the sample surface was about 20 μm. To eliminate possible stray signals, we first measured the reference signal $I_0$ outside the sample and then the signal $I$ transmitted through the sample. The absorption spectrum was calculated by the standard method, from the formula $I = I_0 \exp(-\alpha d)$, where $d$ is the sample thickness and $\alpha$ is the optical absorption coefficient.

The X-ray structural studies were performed under high pressures up to 65 GPa at room temperature in a diamond anvil cell. The sample was $NdFeO_3$ powder obtained by grinding a single crystal in an agate mortar. The diameter of the diamond anvils was 400 μm, and the diameter of the hole in the tungsten gasket was about 120 μm. The pressure-transmitting medium was the same PES-5 liquid. One third of the active volume of the cell was filled with the sample, and two thirds, with the PES-5 liquid. The high-pressure cell allowed the detection of diffraction reflections up to the angles $2\theta = 25°$. The X-ray source radiation was a generator with a molybdenum rotating anode and with a special focusing system [11]. The spectra were measured in the transmission geometry by a two-dimensional detector of the Image-Plate type.

For the pressure measurements, including the estimate of the pressure gradient from the sample diameter, we used the ruby fluorescence shift. The gradient was found to be no higher than 4–5 GPa at maximal pressure.

## 3. RESULTS AND DISCUSSION

*3.1. Optical absorption spectra.* The optical spectra of the $NdFeO_3$ single crystal exhibit rather wide absorption bands corresponding to the *d–d* optical transitions of the $Fe^{3+}$ ion in the crystal ligand field (Fig. 1). At normal pressure, the shape of the spectrum coincides with those obtained previously in [12, 13]. Narrow peaks corresponding to the *f–f* transitions of the $Nd^{3+}$ ions are observed at the background of broad bands [12]. It was found that the energy pressure coefficients characterizing these transitions are approximately two orders of magnitude smaller than the pressure coefficients of the absorption lines corresponding to the *d–d* transitions of the $Fe^{3+}$ ions. In rare-earth ions, the 4*f* shells lie relatively deep, and the size of their wave functions is much smaller than the interionic distances; therefore, their energies weakly depend on pressure. For example, for the *f–f* transitions ${}^4I_{9/2} \longrightarrow {}^2H_{11/2}$, the pressure slope is –0.26 meV/GPa.

The samples remain transparent for wavelengths up to ~8 μm. At normal pressure, below the absorption

edge, which occurs at ~ 2.4 eV, three broad absorption peaks are observed with maxima at (2.29 ± 0.02), (1.73 ± 0.02), and (1.23 ± 0.01) eV [12]. Two broad bands at ~1.23 and ~1.73 eV are caused by the $Fe^{3+}$ $^6A_1 \longrightarrow {}^4T_1$ and $^6A_1 \longrightarrow {}^4T_2$ transitions in the crystal ligand field (octahedral oxygen environment) [12, 13]. The third band near 2.29 eV should correspond to the $^6A_1 \longrightarrow {}^4E_1$, $^4A_1$ transitions, but it is not observed at atmospheric pressure because it lies under the optical absorption edge [12]. Only when the pressure grows does this band shift to the transmission region and become observable.

We found that, as the pressure increases, the energies of all *d*–*d* transitions, namely, $^6A_1 \longrightarrow {}^4E_1$, $^4A_1$; $^6A_1 \longrightarrow {}^4T_2$; and $^6A_1 \longrightarrow {}^4T_1$, linearly decrease (Fig. 2) and their pressure coefficients are –(16.5 ± 0.7), –(9.5 ± 0.7), and –(10.69 ± 0.4) meV/GPa, respectively (see table). The optical absorption edge shifts somewhat slower, with a pressure coefficient of –(6.94 ± 1.62) meV/GPa. However, at $P$ = 37.5 GPa, the absorption edge exhibits a jump from ~2.2 to ~0.75 eV, which testifies to the electronic transition of the insulator-to-semiconductor type. A similar transition was observed by us in $LuFeO_3$ [7].

As a rule, the $Fe^{3+}$ ion in the octahedral environment does not exhibit any strong absorption in the visible range. Therefore, the strong absorption in oxides is attributed to the charge transfer $d^n \longrightarrow d^{n+1}\underline{L}$, where $n$ = 5 and $\underline{L}$ is a hole in the oxygen $p$ band [12–14]. From the theoretical point of view, rare-earth orthoferrites are the strongly correlated electronic systems, in which, according to the Mott–Hubbard model, the gap Δ formed in the excitation spectrum due to the ligand-to-$Fe^{3+}$ charge transfer is smaller than the Coulomb interaction energy $U$ [15]. For example, for $LaFeO_3$, the parameters of the model determined from the X-ray and UV photoemission data are Δ = (2.4 ± 0.7) eV and $U$ = (7.4 ± 0.7) eV [16].

We have established that the quality of the photoluminescence spectra measured in our experiment is impaired by the presence of the contribution from the diamond anvils. Nevertheless, we can conclude that, at room temperature, the spectrum of a $NdFeO_3$ single crystal consists of a single broad line whose maximum (~2.1 eV) is close to the optical absorption edge. In the pressure range $P$ < 27 GPa, this spectrum weakly depends on pressure.

*3.2. Equation of state V(P).* The evolution of the X-ray diffraction patterns obtained for $NdFeO_3$ powder in the pressure range up to $P$ = 65 GPa is shown in Fig. 3. As the pressure increases, all peaks shift toward greater angles and become broader (presumably, because of the pressure gradient growth). In the pressure interval $P$ ~ 35–38 GPa, some peaks disappear, indicating a structural transition. The measurements under decreasing pressure revealed a hysteresis in the region of this transition, which means that the transition is of the first order.

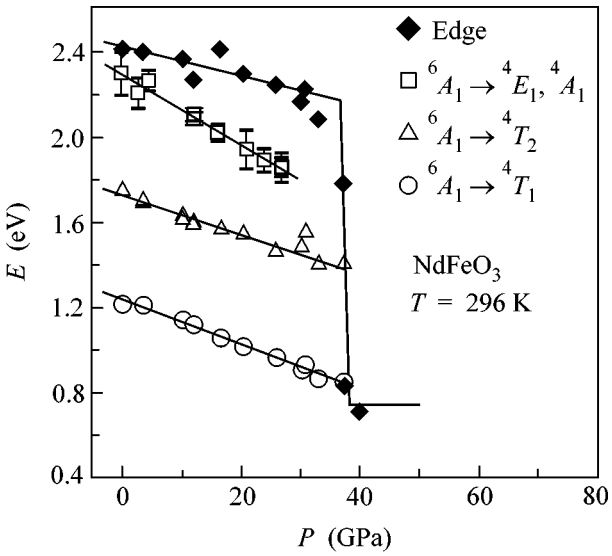


**Fig. 2.** Pressure dependences of energy for the *d*–*d* transitions of the $Fe^{3+}$ ion ($^6A_1 \longrightarrow {}^4E_1$, $^6A_1$; $^6A_1 \longrightarrow {}^4T_1$; and $^6A_1 \longrightarrow {}^4T_2$) and the pressure dependence of the optical absorption edge for $NdFeO_3$ at room temperature. The dots represent experimental points, and the solid lines show the linear approximation.

Figure 4a shows the pressure dependences of the unit cell parameters *a*, *b*, and *c*. At $P$ ~ 25 GPa, the parameters *a* and *b* become equal, and, at $P$ ~ 35 GPa, the parameters *a* and *c* decrease in a jumplike manner. In the pressure interval 60–65 GPa, an anisotropy of compressibility is observed: the *b* axis slightly expands while the *a* axis continues to shorten. The transition is characterized by the presence of two-phase region (see Fig. 4b): upon loading, the X-ray reflections from the low-pressure (LP) phase can be traced up to 42 GPa, and when the pressure decreases, the high-pressure (HP) phase is retained down to 30 GPa. With allowance for the pressure gradient, the hysteresis is equal to approximately 6 GPa.

Parameters of the optical absorption spectra of a $NdFeO_3$ single crystal at normal pressure at room temperature

| Transition | Energy at normal pressure (eV) | Pressure coefficients $dE/dP$ (meV/GPa) |
|---|---|---|
| Absorption edge | 2.42 ± 0.03 | –6.94 ± 1.62 |
| $^6A_1 \longrightarrow {}^4E_1, {}^4A_1$ | 2.29 ± 0.02 | –16.5 ± 0.7 |
| $^6A_1 \longrightarrow {}^4T_2$ | 1.73 ± 0.02 | –9.5 ± 0.7 |
| $A_1 \longrightarrow {}^4T_1$ | 1.23 ± 0.01 | –10.69 ± 0.4 |

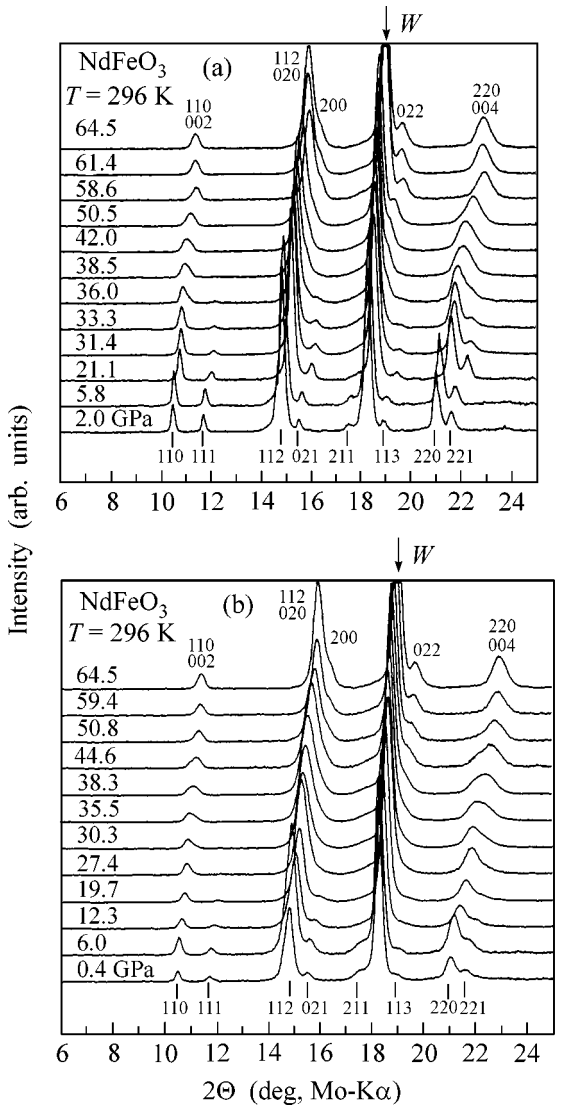


**Fig. 3.** Evolution of the X-ray diffraction patterns for $NdFeO_3$ under (a) increasing and (b) decreasing pressure.

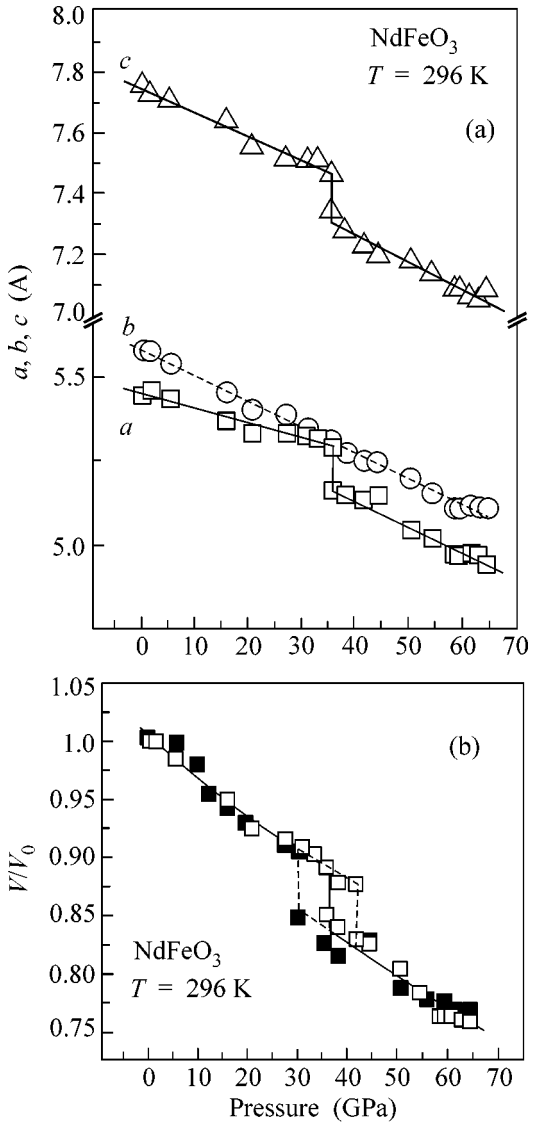


**Fig. 4.** Dependences of (a) the unit-cell parameters and (b) the reduced volume of the unit cell of $NdFeO_3$ on hydrostatic pressure. In plot (b), the empty squares correspond to increasing pressure and the full squares, to decreasing pressure.

Figure 4b shows the dependence of the relative unit-cell volume, $V/V_0$ on pressure. The experimental dependence was approximated by the equation of state $V(P)$ in the Birch–Mournagan form, which was used to calculate the bulk elastic modulus $B_0$ at the fixed value of its derivative $B_0' = 4$. For the initial LP phase, we found $B_0 = 244 \pm 4$ GPa. After the transition to the HP phase, this value was practically retained: $B_0 = 239 \pm 4$ GPa; the mean approximation error was equal to 3.7 GPa. At the structural phase transition near $P \sim 37$ GPa, the unit-cell volume was found to exhibit a jump of ~ 4%.

The structural change under pressure mainly refers the variation of the tilt angle φ of the oxygen octahedron axis with respect to the *c* axis and the decrease in the Fe–O interionic distance. Preliminary calculations showed that, upon the LP⟶HP transition, the tilt angle φ increases from ~151° to ~ 167°, while the Fe–O distances decrease to 1.82 Å along the *c* axis and to 1.79 and 1.89 Å in the basal plane. In the new HP phase, the orthorhombic symmetry is retained, but the (*hhl*) reflections with odd indices *l* disappear, indicating that the symmetry rises to the body-centered one. This is caused by the change in the tilt of the octahedra in the new structure and by the increase in the O–Fe–O bond angles. A similar change in the perovskite structure was observed for $CaTiO_3$ with increasing temperature [17]. The structure of the new phase will be described in more detail in a future publication.

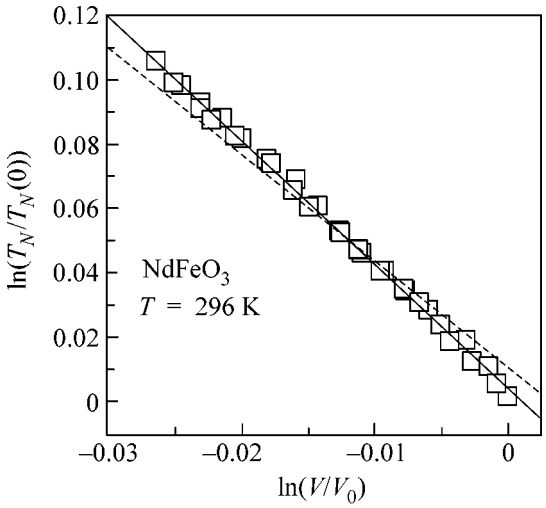


**Fig. 5.** Dependence of the Néel temperature $T_N$ on the unit-cell volume of $NdFeO_3$ on a logarithmic scale. The solid line shows the linear fitting to experimental points, and the dashed line corresponds to $\varepsilon = 10/3$ in the Bloch model.

*3.3. Dependence of the exchange integral on the unit-cell volume.* Anderson [18] showed that, in antiferromagnetic oxides with a superexchange, $T_N$ is proportional to the exchange integral $J$. Using the dependence $V(P)$ obtained for $NdFeO_3$ and the dependence $T_N(P)$ obtained by us earlier [6], it is possible to verify the Bloch empirical relation $J \propto V^{\varepsilon}$ (where $\varepsilon = -10/3$) proposed for transition oxides [19]. For this purpose, we plotted the logarithm of $T_N$ reduced to zero pressure versus the logarithm of the reduced volume $V$ (Fig. 5). The linear approximation of the resulting dependence with allowance for the relation $J \propto T_N \propto V^{\varepsilon}$ gave $\varepsilon = (\partial \ln J/\partial \ln V) = (\partial \ln(T_N)/\partial \ln V) = -(3.8 \pm 0.1)$. Although this value of $\varepsilon$ is somewhat greater than the Bloch value ($\varepsilon = -10/3$), it is in a fairly good agreement with the Bloch model.

## 4. CONCLUSIONS

We can conclude that, within the experimental error, the pressure corresponding to the structural transition coincides with the pressure at which the electronic transition was detected by the jump of the optical absorption edge. It should be noted that, in the high-pressure phase, the optical gap does not drop to zero but takes on a value typical of semiconductors. This fact indicates that the structural and electronic transitions do not lead to the insulator-to-metal transition but only transform the orthoferrite to the semiconductor state. Thus, from the viewpoint of electronic structure, the transition observed in $NdFeO_3$ at 37 GPa is an insulator-to-semiconductor transition.

In the pressure region near ~40 GPa, the structural transitions were recently observed in the $LaFeO_3$ [10] and $PrFeO_3$ [20] orthoferrites, in iron borate $FeBO_3$ [21], and in hematite $Fe_2O_3$ [22]. According to the Mössbauer spectroscopy data, these transitions are accompanied by a magnetic moment collapse due to the $Fe^{3+}$ transition from the high-spin state $S = 5/2$ to the low-spin state $S = 1/2$. Presumably, the electronic transition observed in $NdFeO_3$ in our experiments is also associated with spin crossover ($S = 5/2$) $\longrightarrow$ ($S = 1/2$) in iron ions and implies the transition to a magnetically disordered state at room temperature (magnetic-to-nonmagnetic transition).

We found that the crystal structures of the low-pressure and high-pressure phases have identical elastic properties. The bulk moduli $B_0$ of these phases, which were calculated from the compressibility of the unit cell, proved to be virtually equal. The structural transition is accompanied by a considerable hysteresis with a two-phase region extending over 6–10 GPa. The main structural features of the HP phase include a decrease in the Fe–O interionic distances, a change in the tilt of the oxygen octahedra with respect to the $c$ axis, and an increase in the O–Fe–O bond angles; presumably, these features are responsible for the higher symmetry of this phase.

We are grateful to Professor L.N. Dem'yanets for growing the $NdFeO_3$ single crystals used in our experiments and to Professor Peter Yu (University of California, Berkeley, CA) for stimulating the optical studies at high pressures. The work was supported by the Russian Foundation for Basic Research (project no. 02-02-17364a) and the Program "Strongly Correlated Electrons" of the Physical Science Division of the Russian Academy of Sciences.

## REFERENCES

1. S. Geller, J. Chem. Phys. **24**, 1236 (1956).
2. M. Marezio, J. P. Remeika, and P. D. Dernier, Acta Crystallogr. B **26**, 2008 (1970).
3. I. S. Lyubutin, T. V. Dmitrieva, and A. S. Stepin, Zh. Éksp. Teor. Fiz. **115**, 1070 (1999) [JETP **88**, 590 (1999)].
4. V. E. Naĭsh and E. A. Turov, Fiz. Met. Metalloved. **11**, 161 (1961); Fiz. Met. Metalloved. **11**, 321 (1961).
5. E. A. Turov and V. E. Naĭsh, Fiz. Met. Metalloved. **9**, 10 (1960).
6. A. G. Gavrilyuk, G. N. Stepanov, I. S. Lyubutin, *et al.*, Zh. Éksp. Teor. Fiz. **117**, 375 (2000) [JETP **90**, 330 (2000)].
7. A. G. Gavriliuk, G. N. Stepanov, I. S. Lyubutin, *et al.*, Hyperfine Interact. **126**, 305 (2000).
8. I. S. Lyubutin, T. V. Dmitrieva, A. S. Stepin, *et al.*, Izv. Ross. Akad. Nauk, Ser. Fiz. **65**, 969 (2001).
9. A. G. Gavriliuk, G. N. Stepanov, I. A. Trojan, *et al.*, Mater. Res. Soc. Symp. Proc. **499**, 393 (1998).
10. G. R. Hearne, M. P. Pasternak, R. D. Taylor, and P. Lacorre, Phys. Rev. B **51**, 11495 (1995).

11. A. G. Gavriliuk, I. A. Trojan, R. Boehler, *et al.*, Pis'ma Zh. Éksp. Teor. Fiz. **75**, 25 (2002) [JETP Lett. **75**, 23 (2002)].
12. D. L. Wood, J. P. Remeika, and E. D. Kolb, J. Appl. Phys. **41**, 5315 (1970).
13. K. A. Wickersheim and R. A. Lefever, J. Chem. Phys. **36**, 844 (1962).
14. F. G. Kahn, P. S. Pershan, and J. P. Remeika, Phys. Rev. **186**, 891 (1969).
15. J. Zaanen, G. A. Sawatsky, and J. W. Allen, Phys. Rev. Lett. **55**, 418 (1985).
16. A. E. Bocquet, A. Fujimori, T. Mizokawa, *et al.*, Phys. Rev. B **45**, 1561 (1992).
17. X. Liu and R. C. Liebermann, Phys. Chem. Miner. **20**, 171 (1993).
18. P. W. Anderson, Phys. Rev. **115**, 2 (1959); Solid State Phys. **14**, 99 (1963).
19. D. Bloch, J. Phys. Chem. Solids **27**, 881 (1966).
20. W. M. Xu, O. Naaman, G. Kh. Rozenberg, *et al.*, Phys. Rev. B **64**, 094411-1 (2001).
21. V. A. Sarkisyan, I. A. Troyan, I. S. Lyubutin, *et al.*, Pis'ma Zh. Éksp. Teor. Fiz. **76**, 788 (2002) [JETP Lett. **76**, 664 (2002)].
22. M. P. Pasternak, G. Kh. Rozenberg, G. Yu. Machavariani, *et al.*, Phys. Rev. Lett. **82**, 4663 (1999).

*Translated by E. Golyamina*

JETP Letters, Vol. 77, No. 11, 2003, pp. 625–630. Translated from Pis'ma v Zhurnal Éksperimental'noĭ i Teoreticheskoĭ Fiziki, Vol. 77, No. 11, 2003, pp. 753–758.


# Molecular Self-Organization of $Ho^{3+}$ Impurity Ions in Synthetic Forsterite

**A. V. Gaĭster[1], E. V. Zharikov[1], A. A. Konovalov[2], K. A. Subbotin[1], and V. F. Tarasov[2]**

[1] *Laser Materials and Technology Research Center, Institute of General Physics, Russian Academy of Sciences, Moscow, 119991 Russia*

[2] *Zavoĭskiĭ Physicotechnical Institute, Kazan Scientific Center, Russian Academy of Sciences, Kazan, 420029 Tatarstan, Russia*

**e-mail: tarasov@kfti.knc.ru*

Received May 5, 2003

The structure of paramagnetic centers formed by impurity $Ho^{3+}$ ions in synthetic forsterite is studied by submillimeter EPR spectroscopy in the frequency range 65–200 GHz. It is found that $Ho^{3+}$ enters into the $Mg^{2+}$ sublattice in the form of single ions and dimer centers. The concentration of dimer centers considerably exceeds the concentration of single ions, which points to the molecular self-organization of $Ho^{3+}$ impurity ions into dimers during the growing of the crystals from melt. Possible structures of the dimer center are discussed. The parameters of the effective spin Hamiltonian describing the behavior of the electron–nuclear sublevels of the two lowest electronic levels of the $Ho^{3+}$ $^5I_8$ ground multiplet are determined for a single ion and a dimer center.


PACS numbers: 61.72.Ss; 76.30.Kg

Some of trivalent rare-earth (RE) ions ($Ho^{3+}$, $Tm^{3+}$, $Er^{3+}$, etc.) in dielectric crystals exhibit up-conversion luminescence. Crystals doped with these ions are of interest as active media for solid-state up-conversion visible lasers optically pumped by standard near-infrared diode lasers. In this case, a relatively small distance between the interacting RE ions is one of the most important condition for efficient up-conversion in crystals proceeding through the mechanism of cooperative interaction. This condition is met, in particular, when the crystals contain associations composed of two RE ions occupying neighboring cationic sites (in what follows, such associations will be conventionally called dimers for the sake of brevity). When the distribution of impurity ions over lattice sites is strictly statistical, the ratio of dimer $C_{\text{dim}}$ and single-ions $C_{\text{sing}}$ concentrations is determined by the equation obtained in [1],

$$C_{\text{dim}}/C_{\text{sing}} = 2c(1-c^2), \qquad (1)$$

where $c$ is the total mole fraction of impurity ions in the crystal with respect to the major host component substituted by the impurity ions. In this case, the probability of dimer formation at low RE concentrations typical for most laser materials is also rather low.

Therefore, materials in which the self-organized dimerization of impurities leads to a substantial excess of the concentration of dimer centers over the level determined by Eq. (1) are of special interst to up-conversion lasers.

The occurrence of self-organization of this kind was found, for example, in $CsCdBr_3$ single crystals doped with RE ions [2] or $Cr^{3+}$ ions [3]. The efficiency of up-conversion luminescence with pumping in a region of 1 μm for the $Ho^{3+}$-activated $CsCdBr_3$ crystals with concentrations of only $10^{-1}$–$10^0$ at.% reaches 30% of its value under the direct excitation of the luminescent ion by short-wavelength pumping sources [4, 5].

The mechanism leading to the association of impurity ions into dimers is connected in the case of $CsCdBr_3$ with the condition of the conservation of crystal electroneutrality upon the substitution of trivalent impurity ions for bivalent host cations [6]: trivalent RE ions substitute for bivalent $Cd^{2+}$ cations to form [$Re^{3+}$–$V_{Cd}$–$Re^{3+}$] ($V_{Cd}$ is a vacancy in the cadmium sublattice) associations whose total electric charge equals the charge of three substituted $Cd^{2+}$ ions, so that crystal electroneutrality is conserved.

The formation of impurity–vacancy associates of this kind, which are favorable to a decrease in the dissolution energy of heterovalent impurities, is characteristic of forsterite ($Mg_2SiO_4$) crystals as well [7]. In particular, it was observed previously for $Cr^{3+}$ ions in our work [8].

Note that forsterite significantly outperforms bromides in its thermophysical properties, which alleviates the problem of creating a number of efficient solid-state lasers on its basis operating in various modes. Thus, tunable laser generation was obtained with

**Table 1.** Concentrations of doping impurities in melt

| Sample, no. | Concentration, wt % (mol %) | | |
|---|---|---|---|
| | $Ho_2O_3$ | $Na_2O$ | $Al_2O_3$ |
| 1 | 2.3 (2.0) | | |
| 2 (Figs. 1c, 1d) | 2.3 (2.0) | 0.16 (1.0) | |
| 3 | 4.6 (4.0) | 0.16 (1.0) | 0.19 (1.0) |
| 4 (Figs. 1a, 1b) | 9.1 (8.0) | 0.16 (1.0) | 0.19 (1.0) |

$Cr^{4+}$:$Mg_2SiO_4$ crystals in the range 1.170–1.370 μm [9] with a differential efficiency of up to 38% [10] and power in the continuous-wave mode of up to 1.1 W [11]. Pulses shorter than 20 fs were also obtained [12].

This work reports the observation of the impurity ion dimerization in the holmium-doped forsterite crystals.

## EXPERIMENTAL

The structure of paramagnetic centers formed by $Ho^{3+}$ impurity ions in synthetic forsterite was studied by submillimeter EPR spectroscopy in the frequency range 65–535 GHz on a quasi-optical spectrometer [13]. The experiments were carried out at a sample temperature of 4.2 K in the Voigt geometry. The microwave magnetic-field vector $\mathbf{B}_1$ in all cases was directed parallel to an external magnetic field **B** induced by a resistive electromagnet in the range 0–0.9 T.

The measurements were performed for four samples grown by the Czochralski method. Some samples also contained additional optically inactive and nonparamagnetic $Na^+$ and $Al^{3+}$ ions, which were introduced to improve the solid-state solubility of holmium in forsterite. The concentration of impurity ions in the melt is reported in Table 1.

However, it should be considered that, when forsterite is growing, the RE distribution coefficients between the crystal and the melt do not exceed 0.01–0.02 [14]. Thus, the actual concentrations of holmium in our crystals are approximately two orders of magnitude smaller than its concentrations in the corresponding melts indicated in Table 1, and a direct measurement of the $Ho^{3+}$ concentrations in the crystals by X-ray spectral microanalysis showed that these values do not exceed 0.1 wt %.

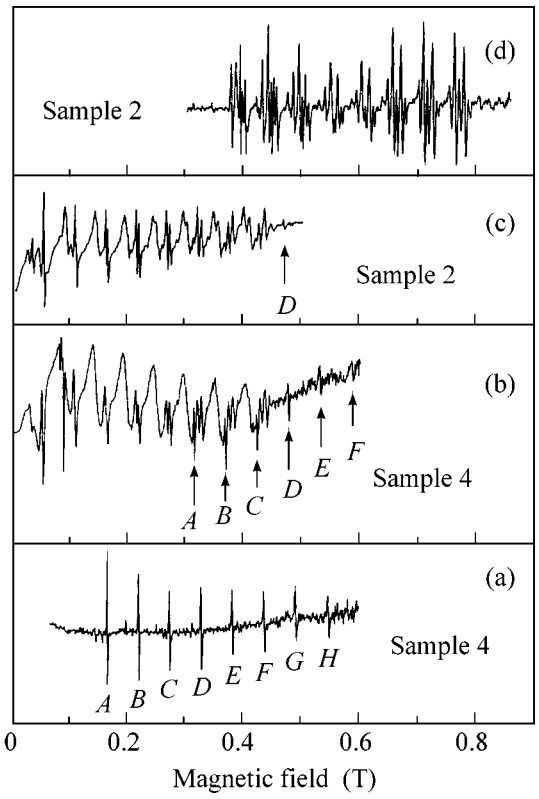


**Fig. 1.** EPR spectra of holmium ions in forsterite at **B** ∥ *b* and $\mathbf{B}_1$ ∥ **B**; frequency ν = (a) 80, (b), (c) 114, and (d) 170 GHz. Arrows in spectra (b) and (c) indicate lines that belong to a single $Ho^{3+}$ ion at position *M*2.

## OBJECTIVE RESULTS

In total, we found four types of paramagnetic centers formed by holmium impurity ions in forsterite. In this paper, we will restrict ourselves to the description and analysis of the results related only to two of them. The structures of the other two centers call for further refinement, and their discussion will be published elsewhere.

Centers of the type discussed in this work were observed in all the samples studied. The EPR spectrum of the center of the first type (from here on, the first center) recorded at a frequency of 80 GHz for the sample indicated in Table 1 under no. 4 is presented in Fig. 1a. It consists of eight narrow equally spaced lines. Measurements of resonance transitions for this center in the frequency range 70–120 GHz showed that the resonance frequencies of hyperfine (HF) components of the spectrum linearly depended on the magnetic field.

The EPR spectrum of the center of the second type is more complicated, and its shape depends on the frequency of recording. Such a spectrum recorded for sample no. 2 (Table 1) at a frequency of 170 GHz in sufficiently strong magnetic fields is given in Fig. 1d. In this spectrum, the resonance signal from the second center is manifested in a pure form. It consists of a large number of narrow lines collected in eight groups. In spite of the sophisticated form of the spectrum and the dependence of its shape on the recording frequency, the measurements carried out at different frequencies (Fig. 2) allowed us to trace the magnetic-field dependence of the frequencies of particular HF components in the spectrum. It was found that this dependence is nonlinear for the second center, and the initial splittings

in a zero magnetic field fall in the range 100–120 GHz. Figures 1b and 1c present the spectra recorded at a frequency of 114 GHz for samples no. 4 and no. 2, respectively. These spectra represent a superposition of signals belonging to both centers mentioned above (however, the individual HF components of the signal from the second center are resolved much worse than in Fig. 1d). The arrows in Figs. 1b and 1c show the lines belonging to the first center.

The study of the orientation dependence of the spectra showed that the first center has two magnetically nonequivalent ion sites in the crystal lattice (two differently directed magnetic *z* axes) and the second site contains four magnetically nonequivalent ion sites. Here, for both of the sites, the angle between the projections of the magnetic *z* axis onto the crystallographic plane *ab* and the *b* axis (from here on, the Pbnm space group is used) equals +29 ± 1° and –29 ± 1°. However, whereas these axes lie strictly in the *ab* plane in the case of the first center, these axes deflect from this plane by an angle of ~ +4 ± 1° and –4 ± 1° for the second center.

## RESULTS AND DISCUSSION

The forsterite structure described in [15] belongs to the orthorhombic system. It consists of a closely packed hexagonal motif of oxygen anions, in which half of the available octahedral voids are occupied by $Mg^{2+}$ ions at two crystallographically nonequivalent positions, ordinarily designated as *M*1 and *M*2 and characterized by the $C_i$ and $C_s$ point symmetry groups, respectively. Each unit cell contains four magnesium positions of each of these types.

The *M*2 positions are somewhat larger than *M*1: the average *M*2–O and *M*1–O bond lengths equal 0.222 and 0.210 nm, respectively [16]. The coordination octahedra occupied by $Mg^{2+}$ ions are arranged as layers parallel to the *bc* plane. The *M*1 octahedra form a linear chain aligned with the crystallographic axis *c*, and the *M*2 octahedra are located at the sides of this chain. The projection of the octahedra of one chain onto the *bc* plane is shown in Fig. 3. The second chain of the occupied octahedra is displaced by *a*/2 and *b*/2 with respect to the first chain and is connected with it by the glide reflection planes *ac* and *bc*.

In the general case, this character of symmetry determines the occurrence of four magnetically nonequivalent ions for position *M*1 and two for position *M*2 [17].

Holmium has one stable isotope $^{165}Ho$ with the nuclear spin $I = 7/2$. Therefore, the EPR HF structure of a single $Ho^{3+}$ ion consists of eight allowed transitions between nuclear sublevels with the same projections of the nuclear moment onto the quantization axis ($\Delta I_z = 0$).

The signal of the first center shown in Fig. 1a has just this shape. With regard to the aforesaid, it may be

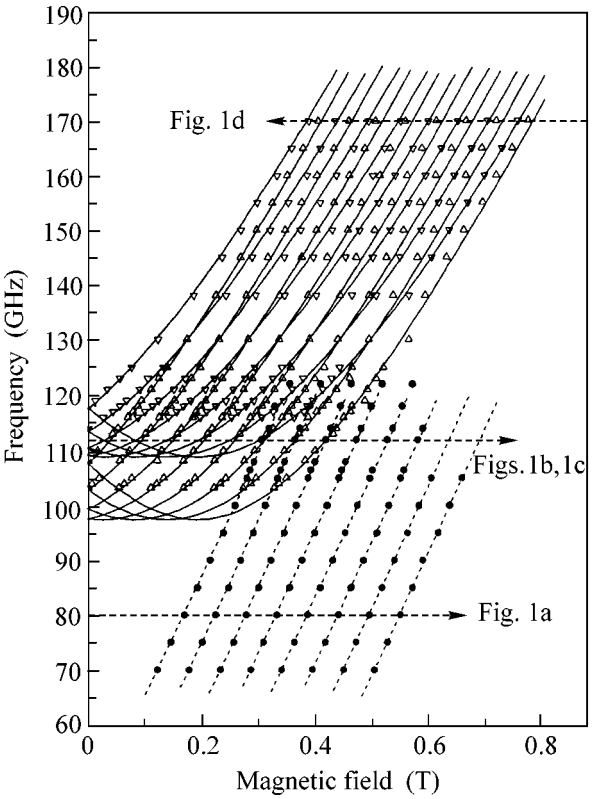


**Fig. 2.** Magnetic-field dependence of frequencies of the HF components of $Ho^{3+}$ EPR spectra at **B** ∥ *b*. Circles and triangles designate experimental points for a single ion and a dimer, respectively. Dashed straight lines and solid lines correspond to calculated dependences for a single ion and a dimer. Arrows show the frequencies of measurements corresponding to Fig. 1.

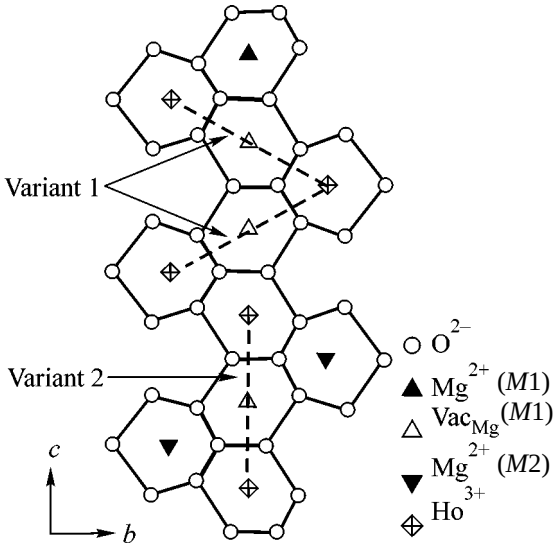


**Fig. 3.** Projections of *M*1 and *M*2 coordination octahedra of the forsterite structure onto the *bc* plane.

**Table 2.** Parameters of the effective spin Hamiltonian for a $Ho^{3+}$ single ion and a $Ho^{3+}$ dimer in forsterite

| | $\Delta$ (GHz) | $g_z$ | $A$ (GHz) | $J$ (GHz) |
|---|---|---|---|---|
| Single ion | 0 | 18.5 ± 0.2 | 12.3 ± 0.2 | |
| Dimer | 51.5 ± 1 | 17.9 ± 0.2 | 11.8 ± 0.2 | 11.4 ± 0.5 |

inferred that the first center found in this work corresponds to the $Ho^{3+}$ ion at the $M2$ position.

For all centers, we observed resonance transitions between the two lowest electronic levels with a zero-field splitting lying in the range 0–110 GHz. Measurements in the range up to 500 GHz did not reveal other resonance transitions. This means that the energy of the third level significantly exceeds the splitting between the two lowest levels. Therefore, in the first approximation, we may consider that the states of the two lowest electronic levels are not mixed in a magnetic field with higher lying states.

One thus can describe the level energies using the effective spin Hamiltonian [18]

$$H_{\text{eff}} = \Delta S_x + g_z \mu_B B_z S_z + A S_z I_z \qquad (2)$$

for the effective electron spin $S = 1/2$ and the nuclear spin $I = 7/2$. Here, the first term corresponds to the initial splitting between the electronic levels in a zero magnetic field, the second term corresponds to the Zeeman energy of electronic levels, and the third term corresponds to the HF interaction between the electron and nuclear spins. The energies of electron–nuclear levels in this case are calculated analytically,

$$W = \pm\frac{1}{2}\sqrt{(g_z \mu_\beta B_z + A I_z)^2 + \Delta^2}. \qquad (3)$$

The eight lines in the spectrum in Fig. 1a correspond to the allowed transitions between the HF sublevels with the same projections of the nuclear spin of the two electronic levels ($\Delta I_z = 0$). The linear field dependence means that $\Delta = 0$ for this center. A least-squares fit of the Hamiltonian parameters (Eq. (2)) gave the values given in Table 2. The theoretical magnetic-field dependences of the resonance frequencies calculated with these parameters for the first center and the corresponding experimental data are presented in Fig. 2. Note that the value of the magnetic moment associated with the states of the two lowest electronic levels $\mu = (g_z/2)\mu_\beta = 9.25\mu_\beta$, where $\mu_\beta$ is the Bohr magneton, is close to the highest possible value $\mu = 10$ for the ground-state $^5I_8$ multiplet of the $Ho^{3+}$ ion. The parameter $A$ can be used to determine the HF coupling constant for the $Ho^{3+}$ ion in forsterite: $A_p = A(g_L/g_z) = 0.83 + 0.02$ GHz, where $g_L = 1.25$ is the Lande $g$ factor. This is close to the value $A_p = 0.812$ GHz obtained for $Ho^{3+}$ in holmium nicotinate [19].

The second center, we believe, has a dimeric structure. The field dependences of the electron–nuclear levels of a dimer can be described using the effective spin Hamiltonian [20]

$$H = \sum H_i - 2JS_{z1}S_{z2}, \qquad (4)$$

where $H_i$ ($i = 1, 2$) is the effective Hamiltonian of individual ions given by Eq. (2) and the right-hand term corresponds to the interaction energy between the ions in a dimer.

The eigenvalue of the Hamiltonian (Eq. (4)) can be conventionally represented as four electronic levels with zero-field energies $-2\Delta$, $\pm J/2$, and $+2\Delta$, consisting of 64 HF sublevels each.

Sixty-four allowed transitions ($\Delta I_{z1} = \Delta I_{z2} = 0$) with nonlinear (as follows from Eq. (3)) magnetic-field dependences of the resonance transition frequencies are possible between the HF components of each pair of electronic levels. Theoretically, in total, we could observe $6 \times 64 = 384$ HF components of resonance transitions.

However, the spectra of $-2\Delta \longrightarrow -J/2$ and $+J/2 \longrightarrow +2\Delta$ transitions, as well as $-2\Delta \longrightarrow +J/2$ and $-J/2 \longrightarrow +2\Delta$ transitions, are superposed on each other because of the closeness of their frequencies. The $-J/2 \longrightarrow +J/2$ transition has a very small splitting in a zero magnetic field that does not fall into the frequency range of our EPR spectrometer. Moreover, the transitions between the electronic levels $\pm J/2$ and $+2\Delta$ has a too low intensity, because the population of the $\pm J/2$ levels is low at 4.2 K. The probability of the $-2\Delta \longrightarrow +2\Delta$ transition is low, and signals of the HF components of this transition also have a rather low intensity.

Thus, in reality, we observe only $2 \times 64$ HF components corresponding to the $-2\Delta \longrightarrow -J/2$ and $-2\Delta \longrightarrow +J/2$ transitions. In our case, both of these transitions are allowed, because the HF coupling energies and energies of interaction between the ions in a dimer are values of the same order of magnitude and the even and odd states with respect to a transposition of particles are mixed. The parameters of the Hamiltonian (Eq. (4)) giving the best fit of the calculated dependences of the resonance frequencies of these transitions to the experimental results are given in Table 2.

The theoretical dependences of the HF components with the same projection of the nuclear spin of the two ions in a dimer calculated with these parameters are shown in Fig. 2 as solid lines. These dependences represent two families of curves corresponding to two transitions. The experimental points assigned to the $-2\Delta \longrightarrow -J/2$ transition are designated by "corner-up" triangles, and points assigned to the $-2\Delta \longrightarrow +J/2$ transition are designated by "corner-down" triangles.

Given the strictly statistical distribution of $Ho^{3+}$ ions in forsterite, the fraction of dimer centers in our samples should be extremely small according to Eq. (1). At the same time, as is evident from the spectra given in Figs. 1b and 1c, the concentrations of dimer centers are not at all lower but, apparently, and on the contrary,

considerably higher than the concentrations of single ions (only if the specific integral intensity of dimer signals does not exceed the similar value for single ions by many orders of magnitude; the probability of this is small, but we cannot exclude such a possibility).

This fact points to the existence of a mechanism in forsterite that leads to the self-organization of $Ho^{3+}$ ions into dimers. It is likely that this mechanism is analogous to the mechanism observed previously for Cd ions in $CsCdBr_3$ [2, 3, 6]. In this case, the dimeric structure must consist of two $Ho^{3+}$ ions and an $Mg^{2+}$ vacancy.

We analyzed two possible structures of such a dimer that provide the best agreement of the calculated energies of dipole–dipole interaction with the experimental value of *J*. These structures are designated in Fig. 3 as "variant 1" and "variant 2."

In the structure of variant 1, $Ho^{3+}$ ions substitute $Mg^{2+}$ at positions *M*2, and a vacancy in the magnesium sublattice *M*1 is located between them. This vacancy violates the mirror symmetry of the crystal field at position *M*2 occupied by impurity ions, which removes the restriction according to which the magnetic axis *z* of the ion at position *M*2 should lie strictly in the *ab* plane or be strictly perpendicular to it. Correspondingly, at an arbitrary deflection of the magnetic axis *z* from this plane, the number of such axes in a unit cell is bred by the crystal symmetry elements up to four. It is this pattern of orientational dependences of the signal of the second center that we observe (see above).

In the case of variant 2, two $Ho^{3+}$ ions are arranged in octahedra of the same linear chain (see Fig. 3). The $Mg^{2+}$ vacancy at position *M*1 is located between these two $Ho^{3+}$ ions. In this case, the dimer is formed by magnetically equivalent ions located in different unit cells, and the number of magnetically nonequivalent dimer centers equals 4, as in the case of single ions at *M*1. The $Cr^{3+}$ ions in forsterite have a similar structure [8].

In addition, as follows from the structural data, octahedra containing the $Ho^{3+}$ ions that form the dimer are separated by a distance of 0.642 or 0.6 nm in the case of variant 1 or 2, respectively. These distances are sufficiently large, which allows us to consider the interaction between the $Ho^{3+}$ ions in the dimer as being of a purely magnetic-dipole nature. Because we know the value and orientation of the magnetic moment of the $Ho^{3+}$ ions from the experiment, the dipole–dipole interaction energy can be calculated by the equation

$$J = \frac{1}{2}\frac{g_z^2\mu_\beta^2}{r^3}(3\cos^2\theta - 1), \qquad (5)$$

where *r* is the distance between the ions, θ is the angle between the axis *z* of the magnetic moment and the radius-vector connecting the ions. The dipole–dipole interaction energy $J_t$ calculated by Eq. (5) for variants 1 and 2 equals 7.44 and 9.46 GHz, respectively. In both cases, it is considerably smaller than the experimental value $J = 11.4$ GHz. The difference between the calculated and experimental values of the dipole–dipole interaction energy can be explained by the displacement of the $Ho^{3+}$ impurity ions towards each other relative to the equilibrium positions of lattice sites. This displacement can be caused by the action of the Coulomb forces associated with the effective negative charge of the magnesium vacancy between these ions. Such a displacement was observed previously for RE dimers of similar structure in $CsCdBr_3$, where the distance between ions decreased by $\delta r \sim 0.07$ and 0.08 nm for $Cd^{3+}$ [2] and $Ho^{3+}$ [21] ions at comparable values of *r*. The value of $\delta r$ for $Ho^{3+}$ ions in forsterite that we calculated from the experimental value of *J* must comprise 0.085 and 0.036 nm for structural variants 1 and 2, respectively.

Thus, based on the available data, one cannot make an unambiguous choice between one or another structure of the dimer center. We believe that variant 1 is more probable. The closeness of the directions of the principal magnetic axis *z* of a single ion at position *M*2 and the ions in a dimer counts in favor of this variant. Moreover, from the viewpoint of the ratio between the sizes of ions $Ho^{3+}/Mg^{2+}$ on the one hand and positions *M*2/*M*1 on the other hand, the predominant location of holmium at *M*1 seems to be unlikely: larger $Ho^{3+}$ ions must prefer more "capacious" positions *M*2.

The smaller difference between the experimental and calculated values of the dipole–dipole interaction energy supports variant 2.

To refine the structure of the observed holmium dimer centers in forsterite, studies by other methods are required, for example, by X-ray diffraction with refinement of the position occupation. However, in order to use this technique effectively, higher concentrations of holmium ions in the crystals are required.

In any case, the high concentration of holmium dimers that we found in forsterite is an encouraging result from the viewpoint of obtaining efficient up-conversion luminescence in forsterite crystals activated by $Ho^{3+}$ ions and further using these crystals as up-conversion converters of IR laser radiation into the visible spectral region.

We are grateful to V.A. Shustov for performing X-ray diffraction experiments.

This work was supported by the Tatarstan Foundation for Research and Development, project no. 06-6.1-143, and the Russian Foundation for Basic Research, project no. 03-02-16374.

## REFERENCES

1. M. Motokawa, H. Ohta, N. Makita, and H. Ikeda, J. Phys. Soc. Jpn. **6**, 322 (1992).
2. G. L. McPherson and L. M. Henling, Phys. Rev. B **16**, 1889 (1977).

3. G. L. McPherson and K. O. Devaney, J. Phys. C: Solid State Phys. **13**, 1735 (1980).
4. M. Mujaji, G. D. Jones, and R. W. G. Syme, Phys. Rev. B **48**, 710 (1993).
5. P. Müller, M. Wermuth, and H. U. Güdel, Chem. Phys. Lett. **290**, 105 (1998).
6. G. L. McPherson and L. M. Henling, Solid State Commun. **19**, 53 (1976).
7. J. A. Purton, N. L. Allan, and J. D. Blundy, Geochim. Cosmochim. Acta **61**, 3927 (1997).
8. G. S. Shakurov and V. F. Tarasov, Appl. Magn. Reson. **21**, 597 (2001).
9. V. G. Baryshevsky, M. V. Korzhik, M. G. Livshits, *et al.*, OSA Proc. Adv. Solid-State Lasers **10**, 26 (1991).
10. V. Petricevic, A. Seas, and R. R. Alfano, OSA Proc. Adv. Solid-State Lasers **10**, 41 (1991).
11. N. Zhavoronkov, A. Avtukh, and V. Mikhailov, Appl. Opt. **36**, 8601 (1997).
12. Z. Zhang, K. Torizuka, T. Itatani, *et al.*, IEEE J. Quantum Electron. **33**, 1975 (1997).
13. V. F. Tarasov and G. S. Shakurov, Appl. Magn. Reson. **2**, 571 (1991).
14. V. B. Dudnikova, E. V. Zharikov, V. S. Urusov, *et al.*, Izv. Vyssh. Uchebn. Zaved., Mater. Élektron. Tekh., No. 2, 11 (2000).
15. J. D. Birle, G. V. Gibbs, P. B. Moore, and J. V. Smith, Am. Mineral. **53**, 807 (1968).
16. Z. D. Sharp, R. M. Hazen, and L. W. Finger, Am. Mineral. **72**, 748 (1987).
17. M. L. Meĭl'man and M. I. Samoĭlovich, *Introduction to Spectroscopy of the Electron Paramagnetic Resonance of Activated Monocrystals* (Atomizdat, Moscow, 1977).
18. P. A. Forrester and S. F. Hempstead, Phys. Rev. **126**, 923 (1962).
19. B. Bleaney, M. J. M. Leask, M. G. Robinson, *et al.*, J. Phys.: Condens. Matter **2**, 2009 (1990).
20. J. M. Baker, S. A. Hutchison, Jr., and P. M. Martineau, Proc. R. Soc. London, Ser. A **403**, 221 (1986).
21. V. F. Tarasov, G. S. Shakurov, B. Z. Malkin, *et al.*, Pis'ma Zh. Éksp. Teor. Fiz. **65**, 535 (1997) [JETP Lett. **65**, 559 (1997)].

*Translated by A. Bagatur'yants*

JETP Letters, Vol. 77, No. 11, 2003, pp. 631–635. From Pis'ma v Zhurnal Éksperimental'noĭ i Teoreticheskoĭ Fiziki, Vol. 77, No. 11, 2003, pp. 759–763.


# Possible Nanomachines: Nanotube Walls as Movable Elements¶

**Yu. E. Lozovik, A. V. Minogin, and A. M. Popov**

*Institute of Spectroscopy, Russian Academy of Sciences, Troitsk, Moscow region, 142190 Russia*

*e-mail: lozovik@isan.troitsk.ru, popov@isan.troitsk.ru*

Received April 14, 2003

Possible types of nanomachines based on many-wall carbon nanotubes and their operation modes are considered. Potential relief and energy barriers for the relative motion of a nanotube wall are studied. Fundamentally new nanomachines based on the threadlike relative motion of nanotube walls are proposed. © *2003 MAIK "Nauka/Interperiodica".*

PACS numbers: 85.85.+j; 61.46.+w

## 1. INTRODUCTION

Progress in nanotechnology in recent decades has given rise to the possibility of manipulation with nanometer-size objects [1]. The principal schemes of nanometer-size machines (nanomachines) where controlled motion can be realized are considered [2]. Thus, the search for nanoobjects that can be used as the movable elements of nanomachines is a very actual challenge in the development of nanomechanics. The low frictional relative motion of carbon nanotube walls [3–5] and the unique elastic properties [6] of these walls allows them to be considered as promising candidates for such movable elements. A set of nanomachines based on the relative sliding of walls along the nanotube axis or their relative rotation is proposed [5, 7–10].

All of these nanomachines correspond to the case where the corrugation of the interwall interaction energy has little or no effect on the relative motion of nanotube walls. However, all carbon nanotube walls have the helical symmetry [11, 12] and this gives the possibility for neighbouring walls of a nanotube to be a nut-and-bolt pair. The present work is devoted to a fundamentally new type of nanomachines where the relative motion of nanotube walls occurs along helical "thread" lines. The possibility of controlling this motion by the potential relief of the interwall interaction energy is considered. A theory for the dynamics of the relative motion of nanotube walls is developed. Possible types of these nanomachines are discussed. Two operation modes for these nanomachines are analyzed: the Fokker–Planck operation mode, where the relative motion of walls occurs as diffusion with drift under the action of external forces, and the accelerating operation mode, where the relative motion of walls is controlled by external forces. The values of the controlling forces corresponding to these modes are estimated.

¶ This article was submitted by the authors in English.

## 2. BARRIERS TO THE RELATIVE MOTIONS OF WALLS ALONG A THREAD LINE

By potential relief we mean the dependence of the interwall interaction energy $U$ of two neighbouring nanotube walls on the coordinates describing the relative position of the wall. Such coordinates are the angle $\phi$ of relative rotation of the wall about the nanotube axis and the length $z$ of relative displacement of the wall along it. Several types of potential relief, including the type where valleys form helical lines, were considered by Dresselhaus *et al.* for a set of double-wall nanotubes [12]. However the barriers to the relative motions of walls along the helical thread lines and to transitions onto neighbouring thread lines have not been previously calculated. Here, we present the first calculation of such barriers. As is discussed below, such nanotubes have some advantages for applications in nanomachines.

The interwall interaction is adopted here to be a 6–12 Lenard–Jones potential $U = 4\epsilon((\sigma/r)^{12} - (\sigma/r)^6)$ with parameters $\epsilon = 2.968$ meV and $\sigma = 3.407$ Å (see [12]). The walls are considered to be rigid. Account of the wall deformation is not essential for the shape of potential relief both for double-wall carbon nanotubes [13] and nanoparticles [14]. The length of the longer inner wall is chosen so that all pairs of atoms with interatomic distances within the cutoff distance are taken into account.

The walls of a double-wall nanotube are commensurate if the ratio of wall unit cell lengths is a rational fraction and incommensurate otherwise. Here, we have studied the threadlike potential relief for a set of nanotubes with both commensurate and incommensurate walls. The threadlike pattern of potential relief arises due to the essential difference between barriers $U_1$ to the relative motion of walls along the thread line and $U_2$ to the transition of the system to a neighbouring thread line ($U_1 \ll U_2$). The threadlike potential relief for a (6,4)@(16,4) nanotube is plotted on Fig. 1.

0021-3640/03/7711-0631$24.00 © 2003 MAIK "Nauka/Interperiodica"

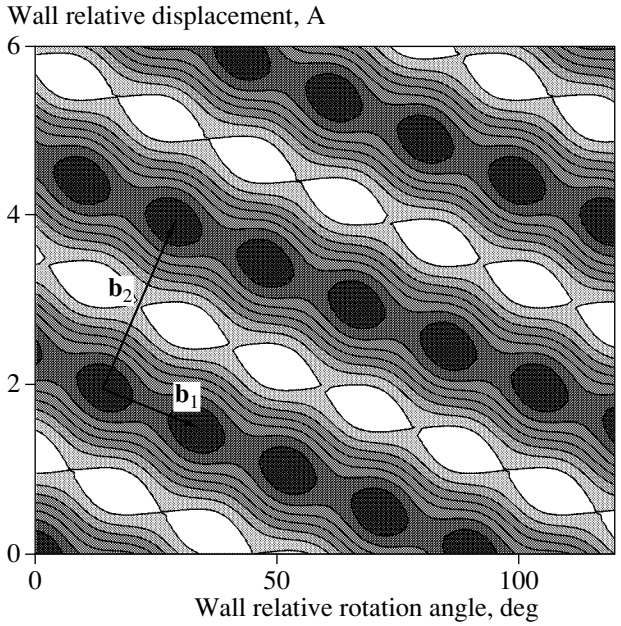


**Fig. 1.** The potential relief of the interwall interaction energy of the (6,4)@(16,4) nanotube as a function of relative displacement of the wall along the nanotube axis and relative rotation angle of the wall about the nanotube axis; $\mathbf{b}_1$ and $\mathbf{b}_2$ are the unit vectors of the lattice formed by minima of the potential relief. The energy is measured from its minimum The equipotential lines are drawn at an interval of $10^{-2}$ meV per atom.

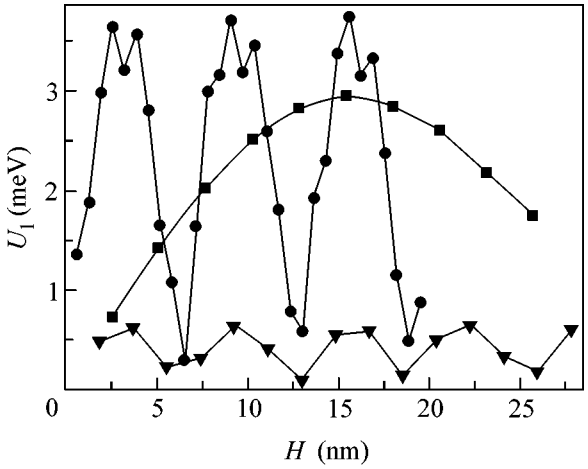


**Fig. 2.** The dependence of the barrier $U_1$ for the relative motion of walls along the thread line on the length $H$ of the outer wall for nanotubes with incommensurate walls. Filled circles, filled triangles, and filled squares correspond to (6,4)@(16,4), (8,2)@(12,8), and (8,2)@(17,2) nanotubes, respectively.

The barriers to any kind of relative motion of incommensurate walls fluctuate near their average value analogously to the sum of functions cos$l$, where $l$ is integer [13]. The dependencies of barriers $U_1$ and $U_2$ on the outer wall length are shown in Figs. 2 and 3, respectively. One can see that barriers change by an order of magnitude for all nanotubes considered, while the outer wall length changes by only few nanometers. Note that these dependencies for both barriers, at least for two of three considered nanotubes, are quasiperiodic functions.

However, the quantity that characterizes the possibility of a double-wall nanotube having a threadlike pattern of potential relief is not the barrier itself but rather the barriers ratio $\gamma = U_2/U_1$. It is natural to call this ratio the relative thread depth. The dependence of the relative thread depth on the outer wall length is shown on Fig. 4. If the average periods of the mentioned quasiperiodic functions are close and oscillations of functions are in phase for both barriers, then the relative thread depth $\gamma$ can be large for substantial changes of the outer wall length. The example of such a possibility is the (8,2)@(12,8) nanotube.

The barriers for any kind of relative motion of commensurate walls with lengths corresponding to an integer number of nanotube elementary cells are given by the relation $U_a = U_u N_u$, where $U_u$ is the barrier per unit cell of the nanotube and $N_u$ is the number of unit cells in the nanotube (the interaction with atoms on the edge of wall is disregarded here). Thus, the barrier $U_a$ for a sufficiently long nanotube is proportional to its length and can make it possible to obtain a given value of the barrier by the choice of the nanotube length. To systemize the search of double-wall nanotubes with commensurate walls that can be a nut-and-bolt pair, the notion of an equivalence class of walls can be introduced [15]. Analysis shows that for some double-wall nanotubes with an integer number of elementary cells, the barriers can be extremely small in comparison with the total interwall interaction energy. The reason for this is the following. The potential field produced by each wall can be expanded on the basis of a harmonics invariant under the symmetry group of the wall [16]. Only harmonics with a symmetry compatible with both walls can contribute to the interwall interaction potential relief $U(\phi, z)$. Therefore, it was found that the barrier for relative wall rotation for some nanotubes is less than the calculation accuracy [17]. One can expect analogous results for the majority of nanotubes with chiral commensurate walls.

## 3. DYNAMICS OF RELATIVE MOTIONS OF WALLS

Let us now study the dynamics of relative motion of double-wall nanotube interacting walls under the action of external forces. One wall is treated as fixed and the motion of the second wall relative to the first is examined. The external forces $\mathbf{F}_i^a$ acting on movable wall atoms does not cause its deformation if these forces have equal magnitudes for each atom and can be

divided into two components $\mathbf{F}_z^a$ and $\mathbf{F}_L^a$ directed along the wall axis and the tangent to its circumference, respectively. The forces of the considered types can have, for example, an electrostatic nature [10] or be applied by a nanomanipulator [5] or laser electric field [7, 8]. Analysis shows that, for the case considered, the motion of one wall of a double-wall carbon nanotube relative to a fixed wall is equivalent to the two-dimensional motion of a particle whose mass equals that of the movable wall in the potential field $U(\mathbf{r})$ and under the action of an external force $\mathbf{F}$, where $\mathbf{r} = (z, L)$, $L = \phi R_1$, $R_1$ is the radius of the movable wall and $\mathbf{F} = (N_a F_z^a, N_a F_L^a)$, and $N_a$ is the number of movable wall atoms.

We consider an ensemble of "particles" whose motion is described by this effective equation of motion, where forces $\mathbf{F}$ have all the properties described above and the potential $U(\mathbf{r})$ corresponds to the lattice as is shown in Fig. 1, for example. The relative motion of walls can be diffusion with drift only in the case of $kT \ll U_1, U_2$, where $U_1$ and $U_2$ are the barriers between minima of $U$ for motion along lattice vectors $\mathbf{b}_1$ and $\mathbf{b}_2$, respectively. We restrict ourselves to the case of $U_1 \ll U_2$, where diffusion is one-dimensional. The probabilities $\omega_1$ and $\omega_2$ of displacements between neighbouring minima in the line of the direction of diffusion and against it, respectively, are approximately given by the Arrhenius formula

$$\omega_1 = \Omega \exp\left(-\frac{U_1 - F_x\delta/2}{kT}\right),$$
$$\omega_2 = \Omega \exp\left(-\frac{U_1 + F_x\delta/2}{kT}\right), \quad (1)$$

where $\Omega$ is a frequency which has the same order of magnitude as the oscillation frequency of the particle near the minimum, $F_x$ is the projection of $\mathbf{F}$ on motion direction, and $\delta$ is the distance between neighbouring minima in the motion direction. Then, the first term of the exponents expansion (therefore, the condition $F_x\delta/2 \ll kT$ is also necessary) is used to obtain the Fokker–Planck equation for a particle concentration $n$:

$$\frac{\partial n}{\partial t} = D\frac{\partial n}{\partial x} + nBF_x. \quad (2)$$

Here $D$ and $B$ are, respectively, the diffusion coefficient and mobility of particles given by

$$D = \frac{1}{2}\Omega\delta^2 \exp\left(-\frac{U_1}{kT}\right), \quad (3)$$

$$B = \frac{\Omega\delta^2}{2kT}\exp\left(-\frac{U_1}{kT}\right). \quad (4)$$

Note that the Einstein ratio $D = kTB$ is fulfilled.

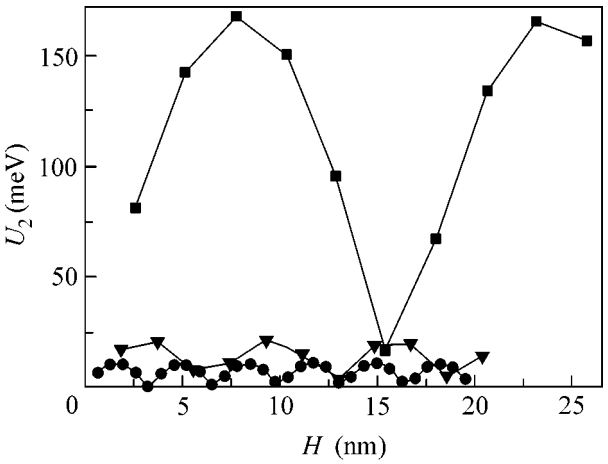


**Fig. 3.** The dependence of the barrier $U_2$ to the transition of the system onto a neighbouring thread line on the length $H$ of the outer wall. Filled circles, filled triangles, and filled squares correspond to (6,4)@(16,4), (8,2)@(12,8) and (8,2)@(17,2) nanotubes, respectively.

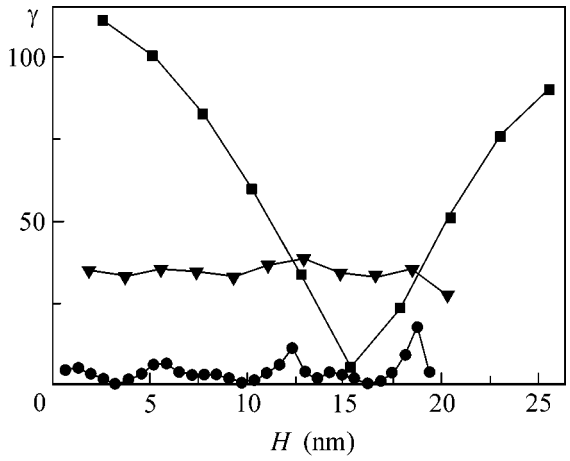


**Fig. 4.** The dependence of the ratio $\gamma = U_2/U_1$, which characterizes the thread depth on the length H of the outer wall. Filled circles, filled triangles, and filled squares correspond to (6,4)@(16,4), (8,2)@(12,8) and (8,2)@(17,2) nanotubes, respectively.

## 4. DISCUSSION

We consider here two types of nanomachines based on the relative motion of nanotube walls. Let us first discuss some possible advantages of applying nanotubes with a threadlike potential relief of the interwall interaction energy in nanomachines where the direction of forces applied on a movable wall does not correspond to the kind of wall motion desired. In the case where the potential relief has a negligible effect on the relative motion of walls, the directions of forces applied on a movable wall must correspond to the direction of

relative motion of walls; namely, if the relative motion of walls is sliding along the nanotube axis, as takes place in constant-force nanosprings [5], gigahertz oscillators [9], and mechanical nanoswitch [10], then the forces applied on a movable wall are bound to be directed along the nanotube axis (first-type forces). If the relative motion of walls is relative rotation, as takes place in nanobearings [7] and nanogears [8], then the forces applied on a movable wall must to be directed along the tangent to its circumference (second type forces).

However, the presence of a threadlike potential relief of the interwall interaction energy remove the restriction on the directions of forces applied on a movable wall. The analysis above shows that relative motion of walls along a helical line of "thread" is possible for both of the discussed types of external forces and any superposition of these. Therefore, the forces of the first type produce not only a relative sliding of walls along the axis but also their relative rotation. Therefore, a nanomachine based on wall motion can operate as a nanowbirligig. The proposed way to convert the forces directed along the nanotube axis into the relative rotation of walls can be used in nanobearings and nanogears. The second-type forces producing a rotational moment gives rise not only to relative rotation but also to relative motion of walls along the nanotube axis. This effect provides the possibility to construct a nanomachine based on a carbon nanotube that is analogous to an old-fashion faucet where rotation of the handle converts into forward motion of a rod.

Here, we also propose a principally new type of nanomachines that may be based on nanotubes with only a threadlike potential relief of the interwall interaction energy. The use of an alternating-sign force to operate the relative position of walls can produce wall motion that is analogous to the motion of an auger in a perforating drill. Such a perforating nanodrill can be used for the modification of a surface in nanometer size.

Another new type of nanodevices which we propose here are based on relative motion of nanotube walls are electromechanical nanodevices. For example, the conductivity of a system consisting of two carbon nanotubes and a fullerene between them [18] can be tuned within orders of magnitude by rotation of one nanotube or its displacement along the axis. This tuning can be controlled with the help of a nanodevice based on the relative motion of nanotube walls. As a result, a variable nanoresistor can be constructed, where a nanotube wall is both a movable element and an element of the electric circuit.

Let us discuss possible operation modes of nanomachines based on relative motion of nanotube walls along a thread line. As we have shown above, in the case when conditions $kT \ll U_1$, $U_2$ and $F_x\delta/2 \ll kT$ are fulfilled, the relative motion of carbon nanotube walls is described by the Fokker–Planck equation (2). Here, the operation mode of a nanomachine based on such a motion is called the Fokker–Planck operation mode. This mode is appropriate for use in a nanomachine if the average $x_{dr} = BF_x t$ that passes by a wall along a helical line of thread as a result of drift is greater than the average distance $x_{dif} = \sqrt{2Dt}$ that passes by this wall as a result of diffusion. This condition is fulfilled for displacements $x_{dr} \gg \delta$, that is, for tens of relative jumps of a wall along a helical thread line between the minima of the interwall potential $U(\mathbf{r})$. Such displacement along a helical line corresponds to less than one revolution of a wall about the nanotube axis or the nanometer displacement along this axis. Although the Fokker–Planck operation mode does not allow precise control of the relative positions of walls, this mode can be used, for example, in a perforating nanodrill for the perforation of layers whose thickness is less than the average displacement $x_{dr}$ of a wall (that plays the role of auger) as a result of drift.

For forces $F_x\delta/2 \gg kT$, the stochastic contribution to relative motion of walls can be neglected. In this case, the relative motion of walls is accelerated and, as discussed above, equivalent to the two-dimensional motion of one particle. Here, the operation mode of a nanomachine based on such motion is called the accelerating operation mode. In this mode, the controlled relative displacement of walls along a helical line of thread for a distance that is less than $\delta$ is possible. This mode can be used, for example, in a variable nanoresistor.

Let us estimate the range of forces that can be used to control the relative motion of carbon nanotube walls in a nanomachine operating both in Fokker–Planck and in accelerating operation modes. Our estimations are made for nanotube (8,2)@(12,8). The ratio of barriers $\gamma = U_1/U_2$ of this nanotube is preserved within the range of 25–40 for all considered lengths of the outer wall. The conditions $kT \ll U_1$, $U_2$ and $F_x\delta/2 \ll kT$ give the maximal force $F_{FP}$ corresponding to the Fokker–Planck mode $F_{FP} \ll U_1/\delta$, where

$$\delta = \frac{a_0}{2}\sqrt{\left(\frac{R_2}{R_1}\right)^2 \cos^2\chi + \sin^2\chi}. \qquad (5)$$

Here, $R_1$ and $R_2$ are the radii of the inner and outer wall, respectively; and $\chi$ is the angle between the helical line of thread and wall circumference.

For nanotube (8,2)@(12,8) we have (1) a value of $\chi$ equal to that of the chiral angle $\theta = 10.89°$ and (2) a magnitude of $U_1 \approx 0.6$ meV corresponding to an outer wall length that equals the length of a unit cell of the wall. As a result, we get $\delta = 1.86$ Å and $F_{FP} \ll 10^{-12}$ N.

Using too high a force in controlling the relative motion of walls in the accelerating mode can give rise to twist-off. The twist-off can occur only if the projec-

tion $F_y$ of the external controlling force on the direction normal to the thread line will satisfy the inequality

$$F_y > \left\langle \frac{\partial U(y)}{\partial y} \right\rangle_y \approx \frac{2U_2}{\delta_y} \quad (6)$$

where $y$ is the relative displacement of the wall in the direction normal to the thread line and $\delta_y$ is the distance between the neighbouringy thread lines

$$\delta_y = \frac{\sqrt{3}a_0}{2}\sqrt{\left(\frac{R_2}{R_1}\right)^2 \cos^2\chi + \sin^2\chi}. \quad (7)$$

For controlling forces greater than $F_{ac} = 2U_2/\delta_y$, the relative motion of walls in the direction normal to the thread line must be taken into account. For controlling forces less than $F_{ac}$, it is sufficient to consider the relative motion of walls only along the thread line; for the nanotube (8,2)@(12,8), on substituting in Eq. (6) $\delta_y$ = 2.23 Å, $U_2$ = 20 meV, and a magnitude of $\chi$ equal to the chiral angle $\theta$, we get $F_{ac} \approx 3 \times 10^{-11}$ N.

## ACKNOWLEDGMENTS

Yu.E.L. is grateful to S.V. Iordanskii and A.Ya. Vul for useful discussions. This work was supported by grants from the Russian Foundation for Basic Research and the Ministry of Science.

## REFERENCES

1. T. Junno, K. Depent, L. Montelius, and L. Samuelson, Appl. Phys. Lett. **66**, 3627 (1995).
2. M. Porto, M. Urbakh, and J. Klafter, Phys. Rev. Lett. **84**, 6058 (2000).
3. M. F. Yu, O. Lourie, M. J. Dyer, *et al.*, Science **287** (5453), 637 (2000).
4. M. F. Yu, B. I. Yakobson, and R. S. Ruoff, J. Phys. Chem. B **104** (37), 8764 (2000).
5. J. Cumings and A. Zettl, Science **289**, 602 (2000).
6. P. Poncharat, Z. L. Wang, D. Ugarte, *et al.*, Science **283**, 1513 (1999).
7. R. E. Tuzun, D. W. Noid, and B. G. Sumpter, Nanotechnology **6**, 52 (1995).
8. D. W. Srivastava, Nanotechnology **8**, 186 (1997).
9. Q. Zheng and Q. Jiang, Phys. Rev. Lett. **88**, 045503 (2002).
10. L. Forro, Science **289**, 560 (2000).
11. C. T. White, D. H. Robertson, and J. W. Mintmire, Phys. Rev. B **47**, 5485 (1993).
12. R. Saito, R. Matsuo, T. Kimura, *et al.*, Chem. Phys. Lett. **348**, 187 (2001).
13. A. N. Kolmogorov and V. H. Crespi, Phys. Rev. Lett. **85**, 4727 (2000).
14. Y. E. Lozovik and A. M. Popov, Chem. Phys. Lett. **328**, 355 (2000).
15. A. V. Belikov, Y. E. Lozovik, and A. M. Popov, Fiz. Tverd. Tela (St. Petersburg) **45**, 1333 (2003) [Phys. Solid State **45** (2003)] (in press).
16. M. Damnjanovic, I. Milosevic, T. Vukovic, *et al.*, Phys. Rev. B **60**, 2728 (1999).
17. M. Damnjanovic, T. Vukovic, and I. Milosevic, Eur. Phys. J. B **25**, 131 (2002).
18. R. Guttierrez, G. Fagas, G. Cuniberti, *et al.*, Phys. Rev. B **65**, 113410 (2002).

JETP Letters, Vol. 77, No. 11, 2003, pp. 636–637. Translated from Pis'ma v Zhurnal Éksperimental'noĭ i Teoreticheskoĭ Fiziki, Vol. 77, No. 11, 2003, pp. 764–765.


# Inductive Excitation of a Two-Dimensional Electron System

**A. V. Chaplik**

*Institute of Semiconductor Physics, Siberian Division, Russian Academy of Sciences, pr. Akademika Lavrent'eva 13, Novosibirsk, 630090 Russia*

*e-mail: chaplik@isp.nsc.ru*

Received April 29, 2003

The possibility of measuring the off-diagonal component of the magnetoconductivity tensor of a two-dimensional electron gas excited by a linear alternating current is discussed. © *2003 MAIK "Nauka/Interperiodica".*

PACS numbers: 73.43.Cd; 74.25.Ha

By the conventional methods of experimental study of the Hall effect (including the quantum Hall effect), either $\rho_{xy}$ and $\rho_{xx}$ in a rectangular sample or $\sigma_{xx}$ in a Corbino disk are measured. Of interest is to develop a method for direct measurement of the $\sigma_{xy}$ magnetoconductivity tensor component. The goal of this work was to suggest an experiment of a new type for measuring $\sigma_{xy}$. The suggested experiment is nonstationary but also low-frequency (i.e., with negligible dispersion of magnetoconductivity).

It is based on the measurement of the response of a two-dimensional electron system to a linear alternating current flowing near it. Let us consider a straight thin superconducting wire placed at distance $\Delta$ from a two-dimensional electron plane $x$–$y$ parallel to the $y$ axis. A current of the given frequency $\omega$ and amplitude $J_0$ flows through the wire. A superconducting wire was selected to exclude from consideration the scalar potential gradient along the wire. In this case, the $y$ component of the vector potential $A_{y_0}$ produced by the current through the wire is the only perturbation. Obviously, it is only a bare perturbation (this is indicated by the index 0), and the shielding effect of the two-dimensional electrons is not taken into account. The wire must remain superconducting in magnetic fields of several tesla, in which the quantum Hall effect occurs. The voltage $V$ at the frequency $\omega$ is measured in the experiment along the $x$ axis between two points on different sides of the perturbing linear current.

The set of Maxwell equations and the constitutive equation relating the current to the field should be solved self-consistently to determine the voltage $V$ taking into account the shielding effect of electrons. It is convenient to introduce the scalar and vector potentials $\varphi$ and $\mathbf{A}$, respectively, and use the continuity equation. Using the Fourier transform for $x$, $y$, and time, we obtain

$$\varphi_{\mathbf{k}\omega} = \frac{2\pi}{\varepsilon R}\rho(\mathbf{k}, \omega)e^{-R|z|}, \tag{1}$$

$$\mathbf{A}_{\mathbf{k}\omega} = \frac{2\pi}{cR}[\mathbf{j}(\mathbf{k}, \omega)e^{-R|z|} + \mathbf{e}_y J_0 e^{-R|z-\Delta|}],$$
$$\mathbf{kj} = \omega\rho, \quad \mathbf{j} = \hat{\sigma}\left(\frac{i\omega}{c}\mathbf{A} - i\mathbf{k}\varphi\right), \tag{2}$$

where $R = \sqrt{k^2 - \varepsilon\omega^2/c^2}$; $\mathbf{j}$ and $\rho$ are the surface densities of the current and the charge, respectively; and $\varepsilon$ is the background dielectric constant. The second term in square brackets corresponds to the perturbing linear current $J_0\delta(x)\delta(z - \Delta)\mathbf{e}_y$, where $\mathbf{e}_y$ is the unit vector along the $y$ axis and $\hat{\sigma}$ is the magnetoconductivity tensor, which has the following components for an initially isotropic medium: $\sigma_{xx} = \sigma_{yy} \equiv \sigma_0$ and $\sigma_{xy} = -\sigma_{yx} \equiv \sigma_1$.

Substituting the expressions for the potentials into Eq. (2) and eliminating $\varphi$ and $\rho$ using the continuity equation, we obtain two linear equations for the current components $j_x$ and $j_y$. The solution for $j_x$ is

$$j_x(\mathbf{k}, \omega) = \frac{2\pi i\omega\sigma_1}{c^2 R}$$
$$\times J_0 e^{-R\Delta}\left[1 + \alpha^2 + \frac{2\pi i\sigma_0\left(k^2 - \frac{2\varepsilon\omega^2}{c^2}\right)}{\varepsilon\omega R}\right]^{-1}, \tag{3}$$
$$\alpha^2 \equiv \frac{4\pi^2}{\varepsilon c^2}(\sigma_0^2 + \sigma_1^2).$$

The expression in square brackets in Eq. (3) (denominator) takes into account the electron shielding effect. If the shielding effect is neglected, the expression in brackets reduces to unity; in the region of Hall plateaus $\sigma_0 \ll \sigma_1 \ll c$, it is close to unity. On the other hand, in the interplateau regions the shielding factor for a frequency on the order of 10 Hz and higher and for a characteristic distance of ~1 cm to the wire can exceed

unity by several orders of magnitude in samples with a sufficiently high mobility.

Further calculations can be performed along two alternative lines. The electric fields $E_x$ and $E_y$ can be calculated from the expressions for the currents $j_x$ and $j_y$ using the equation $\mathbf{j} = \hat{\sigma}\mathbf{E}$ for an infinite homogeneous medium. Then, the potential difference $V$ can be calculated by integrating $E_x$ from $x_1 = -L$ to $x_2 = L$. The alternative possibility is to determine the charge density $\rho(x)$ from the continuity equation and solve the Poisson equation. It is found that the sample is polarized by the perturbation; a dipole moment oscillating with frequency $\omega$ is generated along the $x$ direction. The two methods of calculation lead to the same expression for the $x$ component of the electric field in the plane of the system:

$$E_x(x, z = 0) = \frac{2\pi(1+\alpha^2)\sigma_1 J_0}{\varepsilon c^2}\int_0^\infty \frac{e^{-k\Delta}\cos kx\,dk}{(1+\alpha^2)^2 + \gamma^2 k^2}, \quad (4)$$

$$\gamma \equiv \frac{2\pi\sigma_0}{\varepsilon\omega}.$$

Equation (4) is obtained under the assumption that the electromagnetic wavelength at frequency $\omega$ is considerably greater than the characteristic distances $x$ and $1/\gamma$. It is also assumed that $R = |k|$. In the general case, the expression for the potential difference $V(-L, L)$ is rather cumbersome. However, for $\Delta \ll L, 1/\gamma$ it can be simplified:

$$V(L, -L) = \frac{4\pi^2 J_0\sigma_1}{\varepsilon c^2(1+\alpha^2)}\left[1 - \exp\left(\frac{\varepsilon(1+\alpha^2)\omega L}{2\pi\sigma_0}\right)\right]. \quad (5)$$

In the plateau region, $\sigma_0$ can be smaller than $\sigma_1 = e^2/h \sim 3 \times 10^7$ cm/s by 7–8 orders of magnitude. In this case, for $L \sim 1$ cm the exponential in Eq. (5) is negligible even for $\omega/2\pi \sim 10$ Hz, while the assumption $R = |k|$ is accurate to $(\omega L/2\pi c)^2 \sim 10^{-19}$. Thus, the measured voltage $V$ is mostly proportional to $\sigma_{xy}$. In the interplateau regions, the voltage $V$ (at the same low frequencies) decreases by several orders of magnitude, because $\omega L \ll \sigma_0$, and becomes proportional to the frequency and to the ratio $\sigma_1/\sigma_0$. The order of magnitude of the effect in the region $\sigma_0 \ll \sigma_1$ is $V \sim 0.1$ V for $J_0 = 1$ A ($\varepsilon = 12$), and the values of $\omega$ and $L$ are such that the exponential in Eq. (4) can be neglected.

Let us now consider the applicability of the solution for an infinite homogeneous medium to an actual finite sample. It should be noted that the local relation between the current and the field determined by Eq. (2) with the constant $\sigma$ tensor components breaks down because of the presence of edge channels near the boundaries of a rectangular sample. This difficulty can be avoided by using a Corbino disk instead of a rectangular sample. In this case, the wire should form an almost closed ring (connected to the terminals of an ac generator) placed over the inside part of the structure, i.e., over the two-dimensional electron gas. The $y$ axis is taken along the azimuthal direction and the $x$ axis is taken along the radial direction. The potential difference $V$ is measured between the inner and outer electrodes of the Corbino disk. The results obtained above qualitatively apply in the case under consideration if the width $2L$ of the region occupied by two-dimensional electrons is considerably smaller than its radius, so that a rectangular coordinate system can be used locally. At the same time, the width $2L$ should be large in comparison with the characteristic length $2\pi\sigma_0/\varepsilon\omega$ of electric-field attenuation (see Eq. (4)), to satisfy the zero boundary conditions at infinity that were implicitly used in calculations. In the plateau region at $\sigma_0 \sim 10^{-7}\sigma_1$, this length becomes smaller than $10^{-2}$ cm even for $\omega >$ 10 Hz. To make the obtained formulas applicable in the interplateau regions, where $\sigma_0$ far exceeds the estimate given above, the frequency of the excitating current should be increased correspondingly. It should be noted that there is a considerable frequency margin (7–8 orders of magnitude) to dispersion of $\sigma_0$ and $\sigma_1$.

I am grateful to V.A. Volkov, V.T. Dolgopolov, Z.D. Kvon, and A.A. Shashkin for stimulating discussion. This work was supported by the Russian Foundation for Basic Research (project no. 02-02-16377) and the programs of the Russian Academy of Sciences and the Russian Ministry of Industry and Science.

*Translated by K. Chamorovskiĭ*